UNIVERSIDADE FEDERAL DO RIO GRANDE DO SUL
INSTITUTO DE INFORMÁTICA
PROGRAMA DE PÓS-GRADUAÇÃO EM MICROELETRÔNICA

CAROLINE DOS SANTOS SOARES

Ensemble Monte Carlo Simulation of Hole Transport in Si, Ge and SiGe Alloys

Dissertação apresentada como requisito parcial para a obtenção do grau de Mestre em Microeletrônica.

Orientador: Prof. Dr. Gilson Inácio Wirth

Porto Alegre
2020

CIP – CATALOGING-IN-PUBLICATION

Soares, Caroline dos Santos
Ensemble Monte Carlo Simulation of Hole Transport in Si, Ge and SiGe Alloys / Caroline dos Santos Soares. -- 2020.
86 f.
Orientador: Gilson Inácio Wirth.

Dissertação (Mestrado) -- Universidade Federal do Rio Grande do Sul, Escola de Engenharia, Programa de Pós-Graduação em Microeletrônica, Porto Alegre, BR-RS, 2020.

1. Monte Carlo. 2. Transport of charge carrier. 3. Band structure. 4. Scattering mechanisms. 5. SiGe alloys. I. Wirth, Gilson Inácio, orient. II. Título.

UNIVERSIDADE FEDERAL DO RIO GRANDE DO SUL
Reitor: Prof. Rui Vicente Oppermann
Vice-Reitora: Profa. Jane Fraga Tutikian
Pró-Reitor de Pós-Graduação: Prof. Celso Giannetti Loureiro Chaves
Diretora do Instituto de Informática: Profa. Carla Maria Dal Sasso Freitas
Coordenador do PGMICRO: Prof. Tiago Roberto Balen
Bibliotecária-chefe do Instituto de Informática: Beatriz Regina Bastos Haro

ABSTRACT

Electrical behavior of microelectronic devices can be described by analyzing charge carrier transport. In this work, an Ensemble Monte Carlo code was adapted to simulate hole transport inside silicon, germanium and SiGe alloys. In this simulation, the movement of holes were modeled as free-flight periods that are terminated by scattering events. This simulation technique consists on randomly generating free-flight times for each hole and selecting - based on the hole energy - the scattering mechanism that ends the free-flight. To obtain computational efficiency, in the beginning of the simulation, the scattering rates of all considered processes are calculated and stored in a table as a function of hole energy. The scattering mechanism is randomly selected by comparing the scattering rate saved in the table with a random number, which is generated after the end of the free flight. The scattering processes included in the simulation of hole transport inside these semiconductors are caused by acoustic and nonpolar optical phonon. To simulate the transport of holes inside the SiGe alloys, besides the phonon related mechanisms, the alloy scattering was also incorporated into the code. In the simulator, the valence band of these semiconductors was described by using a three-band approach. Split-off band was considered spherical and parabolic, whereas, both heavy hole and light hole band were described as nonparabolic and warped. The parameters of warping and nonparabolic functions were obtained by fitting the equations that describe each effect to the band structure data obtained by EPM calculations. The simulator was validated by comparing the simulation results with experimental data. The drift velocity of holes in Si at 300K is in excellent agreement with experimental results in a vast range of electric fields. The drift velocity of holes in Ge at 220K successfully agrees with the experimental data. The mobility versus Ge content curve coincides with the experimental one.

Keywords: Ensemble Monte Carlo. Charge carrier transport. Silicon. Germanium. SiGe alloys.

RESUMO

O comportamento elétrico de dispositivos microeletrônicos pode ser descrito pela análise do transporte dos portadores de carga. Nesse trabalho, um código *Ensemble Monte Carlo* foi adaptado para simular o transporte de lacunas em silício, germânio e em ligas SiGe. Nessas simulações, o movimento das lacunas foi modelado como períodos de caminho livre (*free-flight*) que são terminados por eventos de espalhamento. Essa técnica de simulação consiste em gerar randomicamente os tempos de caminho livre para cada lacuna e selecionar – baseado na energia da lacuna – o mecanismo de espalhamento que deve terminar o caminho livre. Para economizar tempo computacional, no início da simulação, as taxas de espalhamento de todos os processos considerados são armazenadas em uma tabela como função da energia da lacuna. O mecanismo de espalhamento é randomicamente selecionado comparando as taxas de espalhamento salvas na tabela com um número aleatório que é gerado depois do fim do caminho livre. Os espalhamentos incluídos na simulação de transporte de lacunas nesses semicondutores são causados por fônons acústicos e ópticos não polares. Para simular o transporte de lacunas nas ligas SiGe, além dos espalhamentos relacionados a interações com fônons, o espalhamento de ligas também foi incorporado no código. No simulador, a banda de valência desses semicondutores foi descrita usando a aproximação de três-bandas. A banda split-off foi considerada esférica e parabólica, enquanto as bandas *light hole* e *heavy hole* foram descritas como não-parabólicas e *warped*. Os parâmetros das funções de não-parabolicidade e *warping* foram obtidos ajustando as equações que descrevem cada efeito aos dados da estrutura de banda calculados por EPM. O simulador foi validado através da comparação dos resultados de simulação com os experimentais. A velocidade de deriva das lacunas em Si a 300K está de acordo com os resultados experimentais para um vasto intervalo de campo elétrico. A velocidade de deriva das lacunas em Ge a 220K concorda altamente com dados experimentais. A curva mobilidade versus concentração de Ge coincide com a curva experimental.

Palavras-chave: Ensemble Monte Carlo. Transporte de portadores de carga. Silício. Germânio. Ligas de SiGe.

LIST OF ABBREVIATIONS AND ACRONYMS

BTE	Boltzmann Transport Equation
CMOS	Complementary Metal Oxide Semiconductor
DFT	Density Functional Theory
EMC	Ensemble Monte Carlo
EPM	Empirical Pseudopotential Method
NBTI	Negative Bias Temperature Instability
OPW	Orthogonalized Plane Wave
p-MOSFET	p-Type Metal-oxide-semiconductor Field-Effect Transistor
RDF	Random Dopant Fluctuations
VCA	Virtual Crystal Approximation

LIST OF SYMBOLS

∇_r	Divergence operator in real space
$\mathbf{v}$	Velocity vector of charge carrier
∇_k	Divergence operator in reciprocal space
$\mathbf{k}$	Charge carrier wavevector
V	Volume of the crystal
Δt	Time step
t_r	Free-flight time
N	Number of charge carrier in the EMC simulation
$\hbar$	Planck constant
$\dot{\mathbf{k}}$	Derivative of the carrier wavevector with respect to time
q	Charge of the carrier
$\boldsymbol{\varepsilon}$	Electric field
ε_0	Vacuum permittivity
Z	Charge of the core
e	Elementary charge
r	Position of an electron
R	Position of a core
m	Electron mass
m_0	Free-electron mass
M	Core mass
p	Momentum of an electron
P	Momentum of the core
H	Hamiltonian
ψ	Crystal wavefunction
U	Effective one-electron potential
E	Crystal energy
$\psi_{\boldsymbol{k}}$	Bloch wave function
$u_{n\boldsymbol{k}}$	Function that has the periodicity of the crystal lattice
H_j'	Perturbed Hamiltonian of a given process *j*
$\Gamma_j[\mathbf{k};\mathbf{k}']$	Transition rate from k to k' of a given process j
$E_{\mathbf{k}}$	Charge carrier energy at a state **k**

$E_{\mathbf{k}'}$	Charge carrier energy at a state **k**′
c	State of the crystal
c′	State of the crystal after scattering
$\mathcal{H}'(\boldsymbol{q}, \boldsymbol{y}, \boldsymbol{r}')$	Coefficients of Fourier series for the perturbed Hamiltonian
N	Number of unit cells
$\mathcal{g}$	Overlap equation
$\Gamma(\mathbf{k})$	Total scattering rate out of state **k**
Δ	The spin-orbit splitting energy
m_{so}	Hole effective mass in split-off band
A	Warping parameter
B	Warping parameter
C	Warping parameter
$g(\theta, \phi)$	Warping angular function
θ	Polar angle of the wavevector
ϕ	Azimuthal angle of the wavevector
β	Nonparabolicity factor
m^*	Effective mass
$\chi(E)$	Nonparabolicity function
$\chi_H(E)$	Nonparabolicity of heavy hole band
$\chi_L(E)$	Nonparabolicity of light hole band
f_H	Angular function of heavy hole dispersion relation
f_L	Angular function of light hole dispersion relation
a	Nonparabolicity parameter
b	Nonparabolicity parameter
c	Nonparabolicity parameter
d	Nonparabolicity parameter
$\mathbf{y}(\mathbf{r})$	Displacement operator
E_{ij}	Acoustic deformation-potential tensor constant
E_{ac}	Acoustic deformation-potential constant
ω	Acoustic phonon angular frequency
ρ	Density
$\mathrm{a}_{\boldsymbol{q}}$	Annihilation operator
$\mathrm{a}^{\dagger}_{-\boldsymbol{q}}$	Creation operator

$\mathbf{e}_q$	Polarization vector
$\mathbf{q}$	Wavevector of the scattered phonon
N_q	Number of phonons
v_s	Sound velocity
v	Velocity of charge carrier
k_B	Boltzmann constant
T	Temperature
$\mathbf{G}$	Reciprocal lattice vector
I_H	Angular integral of heavy hole band
I_L	Angular integral of light hole band
$\Gamma(\mathbf{E})$	Scattering rate as function of energy
D_{op}	Optical deformation-potential constant
E_f	Final energy of a hole scattered by nonpolar optical phonon
ω_{op}	Optical phonon angular frequency
V_0	Alloy averaged potential
V_a	Potential of atom a
V_b	Potential of atom b
x	Ge content in $Si_{1-x}Ge_x$ alloys
V_{alloy}	Alloy scattering potential
Ω_0	Volume of a unit cell
N	Number of scattering mechanisms
rand1	random number uniformly distributed between 0 and 1
rand2	random number uniformly distributed between 0 and 1
rand3	random number uniformly distributed between 0 and 1
Γ_{self}	Scattering rate of self-scattering process
rand4	random number uniformly distributed between 0 and 1
rand5	random number uniformly distributed between 0 and 1
μ	Hole mobility
$\langle v_d \rangle$	Averaged drift velocity

LIST OF FIGURES

Figure 2.1- The processes (drift, diffusion, and scattering) that affect the evolution of the distribution function $f(k,r,t)$. The y-axis shows the change of $f(k,r,t)$ due a charge carrier variation in k, while x-axis shows a change of $f(k,r,t)$ due a charge carrier variation in r... 18
Figure 2.2 - Ensemble Monte Carlo simulation in which an observation time, Δt, is introduced over which the motion of particles. The red squares represent random scattering events. 20
Figure 3.1 - Description of the virtual crystal approximation. ... 31
Figure 3.2 - Fit of the Dresselhaus, Kip and Kittel (1955) curve to the EPM band structure near the top of the heavy hole and light hole bands. ... 34
Figure 3.3 – Silicon heavy and light hole band. In the left side of the graphic, these bands were calculated in the [111] direction and in the right side these bands were calculated in the [100] direction. ... 37
Figure 3.4 – Comparison between the heavy hole band of $Si_{0.2}Ge_{0.8}$ calculated by EPM, by the Dresselhaus, Kip and Kittel (1955) expression and by the analytical expression proposed by Rodríguez-Bolívar, Gómez-Campos e Carceller (2004) ... 39
Figure 3.5 - Flowchart of the main program for EMC simulation. ... 51
Figure 3.6 - Flowchart of free_flight_scatter routine. ... 56
Figure 4.1 – Comparison between the simulated drift velocity of holes in silicon with experimental data. Electric field applied parallel to [100] direction. ... 59
Figure 4.2 - Mean energy of the holes versus electric field for silicon bulk at 300K. ... 60
Figure 4.3 – Occupation of the valence bands vs electric field for Si at 300K. ... 61
Figure 4.4 - Energy of holes in silicon for applied fields of 15, 25, 50, 75 and 100kV/cm 62
Figure 4.5 – Time evolution of drift velocity of holes in silicon for applied fields of 15, 25, 50, 75 and 100kV/cm. It is possible to observe the velocity overshoot and the steady state. 62
Figure 4.6 - Acoustic phonon scattering rates for holes in the heavy hole, light hole and split-off bands in Si. This scattering process is intra-band, which means the initial and the final bands are the same. ... 63
Figure 4.7 - Nonpolar optical phonon scattering rates for holes scattered from the heavy hole band in Si. ... 63
Figure 4.8 - Nonpolar optical phonon scattering rates for holes scattered from the light hole band in Si. ... 64

Figure 4.9 - Nonpolar optical phonon scattering rates for holes scattered from the split-off band in Si. 65
Figure 4.10 - Comparison between the simulated drift velocity of holes in germanium with experimental data. 67
Figure 4.11 – Mean energy of the holes versus electric field for germanium bulk 68
Figure 4.12 - Occupation of the valence bands vs electric field for Ge at 220K. 68
Figure 4.13 - Energy of holes in germanium for applied fields of 15, 25, 50, 75kV/cm. 69
Figure 4.14 - Time evolution of drift velocity of holes in silicon for applied fields of 15, 25, 50, 75kV/cm. 70
Figure 4.15 - Acoustic phonon scattering rates for holes in the heavy hole, light hole and split-off bands in Ge. 70
Figure 4.16 - Nonpolar optical phonon scattering rates for holes scattered from the heavy hole band in Ge. 71
Figure 4.17 - Nonpolar optical phonon scattering rates for holes scattered from the light hole band in Ge. 71
Figure 4.18 - Nonpolar optical phonon scattering rates for holes scattered from the split-off band in Ge. 72
Figure 4.19 – Comparison of the curve hole mobility in $Si_{1-x}Ge_x$ alloys versus germanium content. The scattering potential used in the simulator proposed in this work is equal to 1.2. 75
Figure 4.20 - Comparison of the curve hole mobility in $Si_{1-x}Ge_x$ alloys versus germanium content. The scattering potential used in the simulator proposed in this work is equal to 1.5. 76

LIST OF TABLES

Table 4.1 - Parameters used in Silicon simulations. 66
Table 4.2 - Parameters used in germanium simulations. 73
Table 4.3 – Band structure constants of SiGe alloys used in the simulation of hole transport. In the alloys studied, the Ge content varied from 0.1 to 0.9. 74

CONTENTS

1 INTRODUCTION **14**

1.1 Outline **15**

2 CHARGE CARRIER TRANSPORT IN SEMICONDUCTORS **16**

2.1 Transport Equation **16**

2.2 Monte Carlo Simulation of Charge Transport **18**

2.3 Band Structure **21**

2.3.1 Methods to Calculate Band Structure 24

2.3.2 Band Structure Modeling in Monte Carlo Simulation 25

2.4 Carrier Scattering Mechanisms **27**

2.4.1 General Expression to Scattering Rates 28

3 ENSEMBLE MONTE CARLO SI, GE AND SIGE **31**

3.1 Materials: Si, Ge and SiGe alloys **31**

3.2 Band Structure Model **32**

3.2.1 Warping 33

3.2.2 Nonparabolicity 35

3.3 Scattering Rates **39**

3.3.1 Acoustic Phonon Scattering Rate 40

3.3.2 Optical Phonon Scattering Rate 45

3.3.3 Alloy Scattering Rate 48

3.4 Ensemble Monte Carlo code **50**

3.4.1 Parameter Initialization 51

3.4.2 Creating Scattering Tables 52

3.4.3 Carrier Initialization and Histograms Calculation 52

3.4.4 Generating Free Flight Time 53

3.4.5 Free-flight and Scattering 55

3.4.6 Choosing the Scattering Mechanism 58
3.4.7 Writing Data 58
4 RESULTS **59**
4.1 Silicon Transport Simulations **59**
4.2 Germanium Transport Simulation **67**
4.3 SiGe Transport Simulations **73**
5 CONCLUSION **77**
REFERENCES **79**
APPENDIX A **83**

1 INTRODUCTION

Moore (1975) predicted the number of transistors in integrated circuits would duplicate every two years, in order to achieve this prediction, microelectronic industry has been scaling down transistor dimensions. Moore's law guided the improvements performed on transistors; however, it is expected to be a limit on scaling (THEIS; WONG, 2016). Therefore, instead of miniaturizing CMOS transistor, changing transistor structure, implementing new devices and employing new materials could bring advances in microelectronic industry.

Therefore, employing new materials is an approach to enhance CMOS transistors. In band engineering methods, the silicon band structure is changed to acquire a material in which holes or electrons have mobility higher than they have in silicon (VASILESKA; GOODNICK; KLIMECK, 2010). The addition of germanium in silicon crystalline creates random alloys that have a band structure different from pure silicon. It was showed that the improvement in hole mobility is achieved in SiGe alloys (KASAP; CAPPER 2006; SHIMA, 2003), because of that, this alloy has been studied to be employed in the channel of p-MOSFET. Besides that, it was revealed that the effect of Negative Bias Temperature Instability (NBTI) on SiGe p-MOSFET is smaller than on silicon (FRANCO, J. et al, 2011; WALTL, M. et al, 2017).

To verify whether employing new materials such as SiGe could bring improvements using trial-and-error methodology is highly expensive, because the effect of the concentration of germanium on reliability, on power consumption, would have to be exhaustively tested. To overcome this issue, computational electronics, which simulates charge carrier transport within a semiconductor in order to obtain the electrical behavior of the material, can be an alternative methodology to electrically characterize transistors when a new material is employed.

In this work, a simulation tool to study the transport of holes in SiGe alloys was developed adapting the simulator that was developed by Camargo (2016) in which the transport of hole in pure silicon is simulated. In this method, Boltzmann Transport Equation is solved by Monte Carlo technique where charge carrier transport is modeled as periods of free flight that are interrupted by collision which can change the carrier energy and are responsible to deviate the trajectory of charge carrier. The free-flight time and the scattering mechanism are randomly selected, thus the scattering events that occurs during charge carrier motion inside a semiconductor are described stochastically. Although BTE classically describes the charge carrier transport, the scattering rates are calculated following Fermi's Golden rule.

1.1 Outline

This master thesis is organized into 5 chapters. Chapter 2 starts by discussing the theory of semiclassical transport and the application of the Monte Carlo technique to simulate the transport of charge carrier inside semiconductors. Secondly, the band structure theory and the methodologies employed to calculate it are showed. Finally, the scattering mechanisms responsible for deviating the charge carrier trajectory and the general expression used to calculate the scattering probabilities are depicted.

In Chapter 3, the Ensemble Monte Carlo method used to simulate the transport of holes in silicon, germanium and silicon-germanium alloys is presented in the following sections. Firstly, the methods used to model the band structure of silicon, germanium and SiGe alloys are described. Secondly, the scattering rates of the scattering mechanisms needed to simulate the transport of holes in these materials are presented. Finally, the structure of the code used to simulate the transport of holes in these materials are explained.

In Chapter 4, the results achieved by simulating the transport of holes in silicon, germanium and SiGe alloys are presented. The results obtained in this work are compared with simulation and experimental results, confirming that the proposed simulator is adequate to simulate the transport of holes in these materials. Chapter 5 presents the conclusions of this work and futures perspectives.

2 CHARGE CARRIER TRANSPORT IN SEMICONDUCTORS

Electrical conduction is the transport of charge carrier through a material. In semiconductors, only electrons in conduction band and holes in valence band are free to move through the material, hence, only those particles contribute to the conduction of electrical current (KANO, 1998). The behavior of a semiconductor device can be modeled by tracking the state of each charge carrier and its motion (VASILESKA; GOODNICK; KLIMECK, 2010). Therefore, the carrier transport is essential to specify the operation of any microelectronic device. Although charge carrier transport is described in terms of quantum mechanics, quantum effects only become important when the length scale of the semiconductor device is shorter than the electron phase coherence length (VASILESKA; GOODNICK; KLIMECK, 2010). Otherwise, a semiclassical approach can be used to describe the carrier transport.

In the semiclassical theory of charge carrier transport, electromagnetic fields are driving forces to charge transport (VASILESKA; GOODNICK, 2006). When an external electromagnetic field is applied on the semiconductors, the charge carriers are accelerated in the same direction of the field. While moving in the semiconductor, the charge carriers will interact with phonons, other carriers and crystal defects. These interactions are referred as scattering and when they occur, the trajectory of the charge carrier is deviated, and the energy of the charge carrier may change. Hence, the charge carrier state can be changed by electromagnetic field and by scattering events.

2.1 Transport Equation

Within the semiclassical approach, the probability of finding a charge carrier at time t, with a crystal wavevector **k**, located at the position r is calculated instead of determining the charge carrier state (VASILESKA; GOODNICK; KLIMECK, 2010; LUNDSTROM, 2000). This probability is given by the distribution function of the charge carrier $f(k, r, t)$ (REIF, 1985) which for electrons in equilibrium is the Fermi-Dirac distribution. The distribution function of the charge carrier defines the average state of the carriers in the device (LUNDSTROM, 2000), therefore, when the distribution function is determined during an interval of time, macroscopic properties such as the carrier drift velocity, current and energy can be achieved (JACOBONI; LUGLI, 1989; VASILESKA; GOODNICK; KLIMECK, 2010).

The Boltzmann Transport Equation (BTE) describes the semiclassical transport of the charge carrier. The BTE considers that the variation of the distribution function is caused by

scattering events and by external forces. The BTE can be considered a continuity equation for charge carrier; however, it describes the flow of charge carrier in the reciprocal and real space (LUNDSTROM, 2000). The Boltzmann Transport Equation is shown in equation (2.1) (JACOBONI; LUGLI, 1989).

$$\frac{\partial f}{\partial t} + \mathbf{v} \cdot \nabla_r f + \dot{\mathbf{k}} \nabla_k f = \left. \frac{\partial f}{\partial t} \right|_{scat} \tag{2.1}$$

The first term in the left side of equation (2.1) describes the temporal variation of the distribution function. This term must be zero in steady-state conditions, because in this situation the variations promoted by scattering must be equal to the ones promoted by electromagnetic fields (HAMAGUCHI, 2001).

The second term in the left side of equation (2.1) $\mathbf{v} \cdot \nabla_r f$ is called diffusion term of BTE. This term comes from the variation of the distribution in the real space and is caused by temperature or by concentration gradients. If these gradients are present, there is a diffusion of the carrier in the coordinate space.

The third term in the left side of equation (2.1) is the drift term of BTE. This variation in the distribution function is a result of the change of charge carrier in momentum space $\dot{\mathbf{k}} \nabla_k f$ caused by an external electromagnetic field (VASILESKA; GOODNICK; KLIMECK, 2010).

The term in the right side of equation (2.1) is the scattering term of BTE. The scattering term can be defined as the difference between carriers scattered in and out of the state **k** and is given by (JACOBONI, 2010)

$$\left. \frac{\partial f}{\partial t} \right|_{scat} = \frac{V}{(2\pi)^3} \int \left[f(\mathbf{k}') S(\mathbf{k}', \mathbf{k}) \big(1 - f(\mathbf{k})\big) - f(\mathbf{k}) S(\mathbf{k}, \mathbf{k}') \big(1 - f(\mathbf{k}')\big) \right] d\mathbf{k}' \tag{2.2}$$

Where $S(\mathbf{k}, \mathbf{k}')$ represents the transition rate, which is the probability per unit of time that a carrier in state $\mathbf{k}$ transits to state $\mathbf{k}'$ due to a scattering event, while $S(\mathbf{k}', \mathbf{k})$ represents the transition rate out of $\mathbf{k}'$to state $\mathbf{k}$.

The three processes responsible for the variations of the distribution function are illustrated in Figure 2.1. Showing that the charge carrier flow in the real space due to diffusion of the carrier and flow in the reciprocal space due to scattering and drift processes.

Figure 2.1- The processes (drift, diffusion, and scattering) that affect the evolution of the distribution function $f(k, r, t)$. The y-axis shows the change of $f(k, r, t)$ due a charge carrier variation in k, while x-axis shows a change of $f(k, r, t)$ due a charge carrier variation in r.

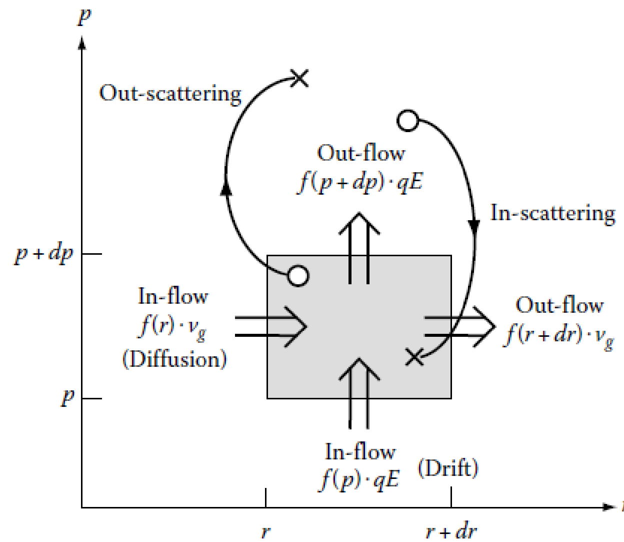

Source: Obtained from Vasileska, Goodnick and Klimeck (2010).

An integral-differential equation is obtained by substituting equation (2.2) into equation (2.1) (JACOBONI; LUGLI, 1989). To solve the BTE in order to determine the distribution function, approximations must be made. Even though using approaches to analytically solve the BTE facilitates the problem, the BTE can be solved directly by applying analytical techniques that simulate the charge carrier movement. The Monte Carlo method is the most popular numerical technique to study the transport of charge carrier inside semiconductors (JACOBONI; LUGLI, 1989).

It is important to notice that in the semiclassical theory of charge carrier transport, the movement of charge carriers between two successive scattering events is described by classical mechanics. However, the scattering rate of each mechanism is derived from quantum theory of scattering (JACOBONI; LUGLI, 1989).

2.2 Monte Carlo Simulation of Charge Transport

Monte Carlo is a numerical technique used to estimate integrals that are complex to be solved analytically (DUNN; SHULTIS, 2012). Monte Carlo can be implemented as a simulation, where quantities can be estimated by directly simulating the process (DUNN; SHULTIS, 2012). Therefore, the transport of charge carrier inside a semiconductor can be simulated by the Monte Carlo method rather than numerically solve the BTE to determine the distribution function (JACOBONI; LUGLI, 1989). In terms of simulating the transport of the

charge carriers inside semiconductors, this numerical technique simulates the motion of the charge carriers subject to external electromagnetic field and to scattering events.

The Monte Carlo method describes the dynamics of the charge carrier as periods of free motion – where the carriers are accelerated by the electromagnetic field, also referred as free-flight time – and instantaneous scattering events, which are responsible for interrupt the free-flight of charge carriers. During the free-flight time, the charge carrier wavevector is only modified by the electromagnetic field, whereas, after the free-flight ends, a scattering event is responsible for changing **k.** The duration of the free-flight time and the scattering mechanism responsible for ending the free-flight are stochastically selected in the Monte Carlo code in accordance with the scattering rates.

The Monte Carlo simulation is discretized in time by time steps – also called observation time – where the carrier properties such energy, band, velocity, wavevector are updated. The time step must be on the order of 10fs to guarantee resolution in the time domain (CAMARGO, 2016). The total time simulated depends on the time needed to reach a steady state; however, the simulated time tends to be of the order of 5-10ps. At the end of the simulation, mean values of interest can be estimated, in addition, the distribution function can be determined.

When tracking the movement of a unique charge carrier inside the semiconductor during a reasonable amount of time, only steady-state properties, such as single particle distribution and average drift velocity, can be statistically estimated. On the other hand, simulating the movement of several carriers allows to estimate the time-dependent evolution of the charge carrier distributions function under the influence of a time-dependent driving force (VASILESKA; GOODNICK, 2006). When the simulation tracks the motion of several charge carriers, it is called an Ensemble Monte Carlo (EMC).

In an EMC algorithm, firstly, some variables that describe the ensemble are defined, such as the temperature, electrical field, number of carrier, the number of bands (holes) or the number of valleys (electrons), the total time of the simulation and the length of the time step. Secondly, the scattering rates as a function of the carrier energy are calculated and stored for each band or valley. After, the EMC algorithm initiates the carrier, which means distributing the carriers in the available bands and attributing them a value of energy based on Boltzmann distribution. The code generates an initial free-flight time (t_r) for each carrier based on the total scattering rate.

After the initialization process, the time loop starts where the free-flight and scattering process may occur. Figure 2.2 represents the time evolution of an EMC simulation. Where the carrier of the simulation is arranged in the vertical axis, the time evolution of each carrier is

showed from the left to the right in the horizontal axis and the red squares represents a scattering event. The time evolution is split in small intervals of time, which is the observation time, where the ensemble movement is synchronized. As can be seen in Figure 2.2, the scattering event may coincide with an observation time, may occur before an observation time, may not occur between two consecutives observation time, besides, more than one scattering may occur during a unique observation time.

Figure 2.2 - Ensemble Monte Carlo simulation in which an observation time, Δt, is introduced over which the motion of particles. The red squares represent random scattering events.

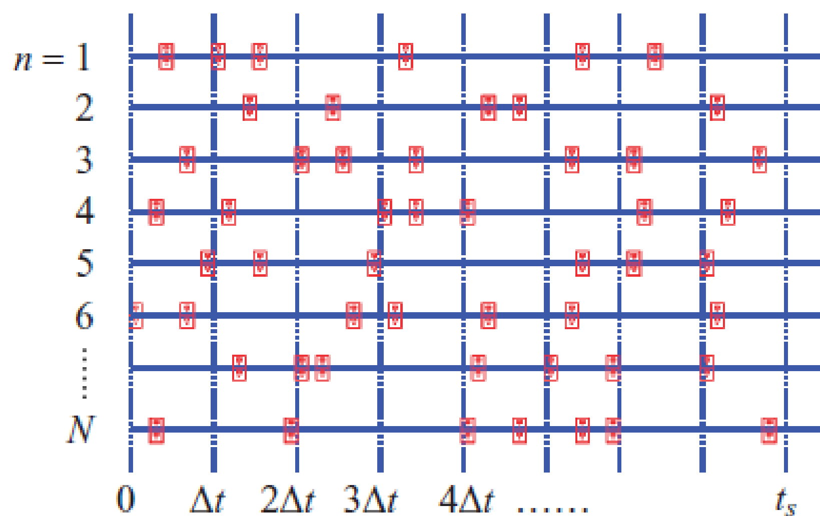

Source: Obtained from Vasileska and Goodnick (2006).

To simulate all these possibilities, in the code, the variables Δt (the observation time) and dte (the time until the next scattering event) are defined. At the beginning of the time loop, the time until the next scattering event (dte) is compared with the observation time. There are two possibilities, dte may be greater than Δt or smaller than Δt.

If dte is larger than Δt: no scattering will occur during Δt, then the carrier will be accelerated by the electric field, changing the wavevector of the carrier. The Δk is calculated and the energy of the charge carrier is calculated based on the new value of k and the code tracks the next carrier.

If dte is smaller than Δt: it means that a scattering event will occur before the next observation time. The carrier will be accelerated by the electric field in an interval of time equal to dte and then will be scattered by the chosen mechanism. The type of scattering that will deviate the trajectory of the ith carrier is chosen based on the ith carrier energy at dte. Based on the scattering mechanism chosen, the energy and the wavevector of the charge carrier are

updated and a new free-flight time is assigned to the carrier. The new free-flight time is compared with the time left until the next observation time.

If the new free-flight time is greater than the time left until the next observation time: no scattering event will occur until the next observation time, the carrier is accelerated by the electric field during the time left until the next Δt, and its wavevector and energy are updated and the code tracks the next carrier.

If the new free-flight time is smaller than the time left until the next observation time: another scattering event will occur before the next observation time. The carrier is accelerated by the electric field in an interval of time equal to new free-flight time, the energy and wavevector are updated. Then all the procedure mentioned above is repeated, the carrier is scattered by the chosen mechanism, then energy and the wavevector of the charge carrier are updated and a new free-flight time is assigned to the carrier.

If all the *N* carriers were updated, the code calculates the velocity of each carrier in each band and then computes the energy, the velocity and the band population of each band. Next, it advances one time-step in time. The loop time goes until the simulation reaches the final time specified in the beginning of the simulation (VASILESKA; GOODNICK; KLIMECK, 2010).

To calculate the change in the charge carrier wavevector caused by the external electric field, the equation (2.3) which relates the time variation of the carrier wavevector ($\dot{\mathbf{k}}$) as a function of the external electric field (ε) must be included into the code. Employing that equation, the wavevector of the charge carrier can be computed.

$$\hbar\dot{\mathbf{k}} = q\varepsilon \tag{2.3}$$

In addition, the energy of an accelerated charge carrier must be changed after a period of free flight, the relation between the energy of the charge carrier and its wavevector is given by the dispersion relation, which is obtained from the material band structure. In the transport simulation of electrons, the dispersion relation of conduction band is necessary, whereas, when simulating the transport of holes, the dispersion relation of valence band is needed. Besides the dispersion relation, it is also needed to calculate the scattering rates as a function of the charge carrier energy and to calculate the charge carrier velocity at each observation time.

2.3 Band Structure

In particle-based simulations, the electrical field is responsible for accelerating the particles between two successive scattering events. However, to extract the velocity and energy

of charge carrier and to calculate the scattering rate for each energy level, band structure information is needed. This section demonstrates that the concept of band structure emerges from the periodic arrangement of the atoms in a crystal and explains its importance to describe the transport of charge carrier inside the semiconductor. The following subsections will present the methods used to calculate the band structure and the approach that will be used in this work to include this information in the Monte Carlo code.

In a crystal, atoms are periodically distributed in space. In such structure, electrons can be classified as valence electrons and core electrons (YU; CARDONA, 2010). Valence electrons are the ones far from the nuclei. Whereas, core electrons are tightly bound to the nuclei, because of that they can be treated as a single particle. The total Hamiltonian of the system is showed in equation (2.4) (COHEN; LOUIE, 2016).

$$\begin{aligned} \mathrm{H}_T = &\sum_i \frac{p_i^2}{2m_i} + \sum_j \frac{P_j^2}{2M_j} + \frac{1}{2}\sum_{i,i'}{}' \frac{e^2}{4\pi\varepsilon_0|r_i - r_{i'}|} + \frac{1}{2}\sum_{j',j}{}' \frac{Z_j Z_{j'} e^2}{4\pi\varepsilon_0|R_j - R_{j'}|} \\ &- \frac{1}{2}\sum_{j,i} \frac{Z_j e^2}{4\pi\varepsilon_0|r_i - R_j|} \end{aligned} \tag{2.4}$$

Where the first and second term are, respectively, the kinetic energy of the valence electrons and of the core. The third term is the Coulomb interaction between valence electrons, the fourth is the Coulomb interaction between cores and the fifth represents the interaction between cores and valence electrons

In equation (2.4), e is the elementary charge, ε_0 is the permittivity of vacuum, m_i, p_i and r_i are, respectively, the mass, momentum operator and position of ith valence electron. While M_j, P_j, R_j and Z_j are, respectively, the mass, momentum operator, position and charge of the jth core. The primed summation means the sum is equal to zero when $i=i'$ and $j=j'$.

A direct solution to equation (2.4) would involve approximately 10^{23} quantum numbers (COHEN; LOUIE, 2016). Because of that, the many-body Hamiltonian cannot be solved without applying simplifications. Besides separating electrons into those two groups, another simplification is the Born-Oppenheimer or adiabatic approximation (COHEN; LOUIE, 2016). In that simplification, the motion of core and valence electrons are treated separately. This assumption is acceptable because the core electrons are heavier than the valence electrons, thus they can be considered static, while valence electrons are lighter, thus they move faster. Therefore, the total Hamiltonian can be split into the core part and the electronic part. In the electronic part, the one that matters to electronic properties, the cores are considered fixed.

The independent electron approximation is another simplification to solve the electronic Hamiltonian, where the electron-electron interactions and the interaction between electrons and core and are represented by an effective one-electron potential, which is a periodic function with periodicity of the crystal lattice (ASCHROFT, 1976). The independent electrons are known as Bloch electrons and each of them is described by a one-electron Schrodinger equation, showed in equation (2.5), where the interaction potential U is the effective one-electron potential. Applying this approach, the one-electron equation can be solved rather than solving the many-body equation (ASCHROFT, 1976).

$$\mathrm{H}\psi = \left(-\frac{\hbar^2}{2m}\nabla^2 + U(r)\right)\psi = E\psi \tag{2.5}$$

Due to the periodicity of the potential, the crystal wavefunction can be described by Bloch wavefunction, equation (2.6), which is chosen to have a form of a plane wave $e^{i\boldsymbol{k}\cdot\boldsymbol{r}}$, where **k** is the Bloch wavevector, times a function that has the periodicity of the crystal lattice $u_{n\boldsymbol{k}}(\boldsymbol{r})$ (ASCHROFT, 1976).

$$\psi_{n,\boldsymbol{k}} = e^{i\boldsymbol{k}\cdot\boldsymbol{r}} u_{n\boldsymbol{k}}(\boldsymbol{r}) \tag{2.6}$$

Substituting the effective potential and the Bloch wave function in the one-electron Schrodinger equation, it is observed that the energy is a continuous function of **k** with periodicity equal to the reciprocal lattice, $E_n(\mathbf{k})$. The n index – which represents the energy level – occurs because there are many solutions for the Schrodinger equation for a given **k** (ASCHROFT, 1976). For each n, the set of $E_n(\mathbf{k})$ is called energy band. The diagram where all the energy bands are displayed forms the band structure.

The band structure of a material presents all the available states of an electron as well as the forbidden states. Regarding electrical conductivity of semiconductors, valence and conduction are the most important bands. Between those two bands there is a range of energy called energy gap where electrons are prohibited from occupying. Valence band is the highest fully occupied band, while the conduction band is the lowest empty one. In semiconductors, charge carriers are electrons in the conduction band and holes in valence band. Although electron is a particle that has negative charge, hole represents the absence of an electron in the valence band (JACOBONI; LUGLI, 1989), hence, it is defined as a quasi particle that has a positive charge.

In semiconductors at 0K there is no vacancy in the valence band nor electron in the conduction band. Therefore, the electrical conduction is negligible. Nevertheless, energy can be transferred to electrons in order to promote electrons in conduction band, creating holes in valence band. Increasing the semiconductor temperature is a method to provide energy to electrons, allowing transition between valence to conduction band. Besides, atomic impurities can be added into semiconductor, using ion implantation technique, to increase the density of one of the two charge carrier (KANO, 1998).

2.3.1 Methods to Calculate Band Structure

All the modern methods used to calculate the band structure are based on finding the effective potential that correctly describes the interactions in equation (2.5) (FERRY, 2013). To determine the band structure of solids, several methods can be employed – which can be classified as *ab initio* or empirical (GONZALEZ, 2001). *Ab initio* methods (Hartree-Fock, Density Functional Theory) make use of approximation to solve the many body Hamiltonian without employing empirical parameters, therefore, no empirical parameters are used to acquire the band structure (VASILESKA; GOODNICK; KLIMECK, 2010). In contrast, there are empirical methods (Empirical Pseudopotential Method, k.p) where the parameters used to describe the interaction potential are obtained by fitting the pseudo-potential to agree with experimental measurements, such as band gap (GONZALEZ, 2001).

These *ab initio* methods use self-consistent procedures in order to get the correct wavefunction, potential and energy levels. While Hartree-Fock method directly calculates the wavefunction and its eigenvalues (MARTIN; REINING; CEPERLEY, 2016), in Density Functional Theory (DFT) all the terms in the Hamiltonian, kinetic energy and the potential, are functionals of the electron density (SÓLYOM, 2010). DFT is based on the Hohenberg–Kohn theorems, which the first one states that electron density determines the ground-state wavefunction and consequently the ground-state expectation value of any observable physical quantity (SÓLYOM, 2010). The ground energy can be obtained using the second theorem, which states that when the energy is a functional of the density, it takes its minimum value at the true ground-state density. These first principle methods are hardly employed to calculate the band structure of crystals or large molecules, because a long time is needed to solve the Hamiltonian (GONZALEZ, 2001).

Since *ab initio* calculations require a long computational time, when it comes to calculate the band structure of crystals, empirical methods are usually employed (GONZALEZ, 2001). Examples of empirical methods widely used are k.p and Empirical Pseudopotential. In

the k.p method, the Hamiltonian is formed by the kinetic energy and the effective potential and two other terms, which one is expressed as the dot product between the wavevector and the momentum (YU; CARDONA, 2010). The energy and the wavefunction at a point ko - usually k_0 is (000) - is calculated, then the terms proportional to k are treated as perturbations (YU; CARDONA, 2010). The band dispersion near any point k_0 can be calculated by expanding the Hamiltonian around k_0. Since the perturbation is proportional to the wavevector, this method is better employed to describe the band structure for small values of the wavevector. The k.p parameters needed to calculate the band structure are inferred from experimental data, usually energy gaps data are used (YU; CARDONA, 2010). Besides calculating the band structure, this method can also provide analytic expressions for effective masses and energy-wavevector dispersion.

In the Empirical Pseudopotential method, the wavefunction is described applying the orthogonalized plane wave (OPW) method, proposed by Herring (1940), where the crystal wavefunction is formulated to be orthogonal to the core wavefunctions. From this approach, the result potential – the pseudopotential - is the sum of the core attractive potential and a short-range non-Hermitian repulsion potential. A methodology to solve the Hamiltonian is expanding the periodic part of the wavefunction and the pseudopotential into Fourier series over the reciprocal lattice, which results in an eigenstate and eigenvalue problem. The size of the matrix and the accuracy of the calculation is determined by the number of reciprocal lattice vectors used to expand the pseudopotential and crystal wavefunction (GONZALEZ, 2001). Usually, these calculations consider the reciprocal lattice vectors up to 10th-nearest neighbor from the origin, which yields into 137 plane waves for a crystal with diamond lattice. In addition, the Spin-orbit interaction can be computed by the EPM method, thus degenerate states can be split.

The dispersion relation (E-k) is highly important when it comes to transport of charge carrier, because the particle kinematics can be determined from the band structure (GONZALEZ, 2001). The next section presents the methods employed to include the band structure information into codes that simulates the transport of charge carrier using the semiclassical approach.

2.3.2 Band Structure Modeling in Monte Carlo Simulation

When it comes to simulate the transport of charge carrier using the semiclassical model, the dispersion relation of conduction band (electrons transport) or valence band (hole transport) is needed to calculate velocity, energy and the scattering probabilities of the charge carrier.

There are two methodologies to describe the band structure in these transport simulations: one is using analytical expressions that describes the dispersion relation based on the effective mass concept and the other is applying full band calculations.

For free electrons, the dispersion relation is given by equation (2.7), where m_0 is the mass of the free charge.

$$E_k = \frac{\hbar^2 k^2}{2m_0} \tag{2.7}$$

Charge carriers that move inside a crystal behave slightly different from free charges carriers because crystal lattice interacts with them. The concept of effective mass was created to consider the effect of the lattice on charge carrier interaction. Due to the crystal lattice interaction, the mass of an electron in vacuum is different from the mass of an electron in conduction band and from the mass of a hole in valence band (KANO, 1998).

In the effective mass approach, the relation between energy and wavevector of a charge carrier inside a semiconductor can be characterized employing an expression similar to equation (2.7), however, in terms of the effective mass instead of the free-electron mass (JACOBONI; LUGLI, 1989). Therefore, the goal of this approach is finding a value or an expression for the effective mass of valence band (holes) or the effective mass of the conduction band (electrons) that correctly relates the energy and wavevector of these bands.

Following this approach, in the region around valleys of the conduction band or around the maximum of the valence band, E(k) can be described as a parabolic or as a non-parabolic function of **k**. When the energy is not correctly described by a quadratic dependence of k, the nonparabolicity occurs (JACOBONI, 2010). In such cases, the nonparabolicity must be included in the effective mass expression by a nonparabolic factor.

In terms of the constant energy surfaces, the band can be classified as spherical, ellipsoidal or warped. The dispersion relation of spherical bands is described in terms of a single effective mass, while the ellipsoidal band must be described by a transverse and longitudinal effective mass. The constant energy surface of a warped band is referred as a spherical "warped", where the warping effect occurs along the [100] and [111] directions (YU; CARDONA, 2010), because of that, the effective mass of warped band is more complex to describe.

In cases where more than one conduction band minimum/valence band maxima are important to describe electrons/holes transport, these other bands are modeled as well,

describing the band structure as a multi-valley or multi-band (VASILESKA; GOODNICK; KLIMECK, 2010). In this approach, the total scattering rates for all mechanisms are written as function of the charge carrier energy.

The second approach incorporates the band structure calculation into the transport simulation in both particle dynamics and scattering routines, because of that, transport simulation that use this method to describe band structure are called full band Monte Carlo simulation. Usually the Empirical Pseudopotential method is employed to perform these calculations. In this approach, the total scattering rates for all mechanisms are written as function of the initial $\mathbf{k}$ and final $\mathbf{k}'$ and stored in a table, because of that, a huge amount of memory is necessary (VASILESKA; GOODNICK; KLIMECK, 2010). Furthermore, this type of simulation is very time consuming.

Therefore, modelling the band structure in terms of the effective mass is usually more efficient, since it is less time and memory consuming. It has been shown that when the effective mass is correctly modeled, the transport simulation results agree with experimental ones (RODRÍGUEZ-BOLÍVAR, 2005; DEWEY;OSMAN, 1993).

2.4 Carrier Scattering Mechanisms

Charge carrier transport is randomly interrupted by scattering events that can modify the energy and momentum of the carrier, deviating its trajectory. When the energy of a charge carrier changes after a scattering event, a state transition occurs, and the scattering is said to be inelastic. Nevertheless, when the energy remains the same, the scattering is said to be elastic.

Charge carrier scattering can be classified in terms of the mechanisms that cause it. A scattering event is caused by the interaction of charge carriers with other charge carrier, defects, and lattice vibrations (phonons). Those mechanism can also be divided into intraband and interband. When the first occurs, initial and final state are in the same band, nevertheless, in an interband transitions the initial and final state are in different bands (VASILESKA; GOODNICK; KLIMECK, 2010).

Charge carrier scattering is due to electrostatic interaction between two charge carriers. This mechanism, that is important when the charge carrier density is high, can be binary, where a charge carrier interacts with another one, or collective, where a charge carrier interacts with the plasma formed by the carriers. The first is understood as a collision between two charge particles and the second regards the influence of all charge carrier in the material on a charge carrier velocity (VASILESKA; GOODNICK; KLIMECK, 2010).

Defect scattering is caused by charged and neutral impurities and by the disorder in the lattice of the alloy material. Ionized impurity scattering occurs when charged impurities, such as dopants, interact with charge carriers by electrostatic potential, because of that, it is also known as Coulomb scattering. On the other hand, neutral impurity scattering occurs when charge carrier interacts with a neutral impurity during its motion, polarizing it; thus, this interaction is an electron–dipole type. This kind of scattering is less effective than the ionized impurity scattering. Its importance is relevant when the semiconductor is very pure or when it operates in low temperature (VASILESKA; GOODNICK; KLIMECK, 2010). Finally, alloy scattering only takes place on alloy semiconductor, such GaAs and SiGe. This type of mechanism is due to fluctuation of the material composition in the crystal lattice.

The phonon scattering occurs due to the displacement of atoms from their equilibrium position, which cause variations in the periodic potential felt by electrons on conduction band and by holes in valence band. Atoms in crystal lattice are not static, they vibrate around their equilibrium position. This vibration is propagated through the crystal, and the quantum particles that transport the vibrational energy are called phonons (HAMAGUCHI, 2001). In terms of their vibrational mode, phonons can be classified as acoustic when atoms move in phase or as optical when two adjacent atoms move out of phase (ASCHROFT, 1976). The displacement of each neighboring atom caused by optical phonon contributes directly to the lattice distortion since they move in opposite directions. However, in the acoustic phonon, neighboring atoms dislocate from their equilibrium position in the same directions; therefore, the strain created by acoustic mode cause the distortion on crystal lattice (VASILESKA; GOODNICK; KLIMECK, 2010; LUNDSTROM, 2000). In addition, phonons can interact electrostatically with charge carriers in a polar semiconductor, where an induced electrical field is created by the distortions caused by phonons (HAMAGUCHI, 2001).

2.4.1 General Expression to Scattering Rates

The scattering events responsible for ending the free flight of a charge carrier are described by quantum mechanics. In the scattering theory, when the charge carrier transit from a Bloch state to another one, the total Hamiltonian is split into the charge carrier Hamiltonian, the crystal Hamiltonian and the perturbation Hamiltonian H', which describes the interaction between the charge carrier and the particle that induces the scattering. The first two are the unperturbed Hamiltonian, which eigenstates are $\mathbf{k}$ and $\mathbf{c}$.

For each scattering mechanism there is a transition rate, which is the probability per unit of time that a charge carrier in state $|\mathbf{k}, \mathrm{c}\rangle$ in a band n transits to an empty state $|\mathbf{k}', \mathrm{c}'\rangle$ in a band m due to the jth scattering process. Using Fermi's Golden rule, where the scattering event is described by the time-dependent perturbation theory of quantum mechanics, the transition rate from a state $|\mathbf{k}, \mathrm{c}\rangle$ in a band n to a final state $|\mathbf{k}', \mathrm{c}'\rangle$ in band m can be expressed by equation (2.8) (VASILESKA; GOODNICK; KLIMECK, 2010; JACOBONI, 2010).

$$\Gamma_j[\mathbf{k}, \mathrm{c}; \mathbf{k}', \mathrm{c}'] = \frac{2\pi}{\hbar}\left|\langle\mathbf{k}', c'\middle|H_j'\middle|\mathbf{k}, c\rangle\right|^2 \delta(E(\mathbf{k}', c') - E(\mathbf{k}, c)) \tag{2.8}$$

In the equation (2.8), $E(\mathbf{k}, c)$ is the energy of the unperturbed state $|\mathbf{k}, \mathrm{c}\rangle$ and $E(\mathbf{k}', c')$ is the energy of the perturbed state $|\mathbf{k}', \mathrm{c}'\rangle$. The delta function in equation (2.8) describes the energy conservation. H_j' is the perturbation Hamiltonian of the jth scattering mechanism, which generally acts on the real space coordinate of the charge carrier (**r**), on the real space coordinate of other charge carrier (**r'**) and on variables that describe the state of the crystal, such as the atom displacement with respect to their equilibrium position (**y**).

In order to calculate the scattering rate of a mechanism, it is convenient to expand the perturbation Hamiltonian of the mechanism into Fourier series, as it is showed in equation (2.9).

$$H'(\mathbf{r}, \mathbf{y}, \mathbf{r}') = \frac{1}{\sqrt{V}}\sum_q \mathcal{H}'(\boldsymbol{q}, \boldsymbol{y}, \boldsymbol{r}')\exp\,(i\mathbf{q}\cdot\mathbf{r}) \tag{2.9}$$

Where $\mathcal{H}'(\boldsymbol{q}, \boldsymbol{y}, \boldsymbol{r}')$ are the coefficients of Fourier Series and V is the crystal volume. Replacing the above expression of H' into the matrix element $\langle\mathbf{k}', c'|H'|\mathbf{k}, c\rangle$ present in equation (2.8), yields

$$\langle\mathbf{k}', c'\middle|H_j'\middle|\mathbf{k}, c\rangle = \frac{1}{\sqrt{V}}\sum_{\mathbf{q}}\langle c'|\mathcal{H}'(\boldsymbol{q}, \boldsymbol{y}, \boldsymbol{r}')|c\rangle \int d\mathbf{r}\psi_{\boldsymbol{k}}^*(\mathbf{r})\exp\,(i\mathbf{q}\cdot\mathbf{r})\psi_{\boldsymbol{k}}(\mathbf{r}) \tag{2.10}$$

The integral in equation (2.10) comes from the matrix elements $\langle\mathbf{k}'\middle|H_j'\middle|\mathbf{k}\rangle$. $\psi_{\boldsymbol{k}}(\mathbf{r})$ is the charge carrier eigenstate, which is describe by a Bloch wavefunction, given by equation (2.11).

$$\psi_{\boldsymbol{k}}(\mathbf{r}) = N^{-1/2}u_{\boldsymbol{k}}(\mathbf{r})\exp\,(i\mathbf{k}\cdot\mathbf{r}) \tag{2.11}$$

Where N is the number of unit cell in the crystal, and the term $N^{-1/2}$ is included to normalize the Bloch wavefunction.

The integral in equation (2.10) can be substituted by a sum of integrals over the crystal cells, which are labelled as j and its position is $\mathbf{R}_j$. Then a change in the variable $r' = r - R$ must be made to result in equation (2.12).

$$I = \sum_j e^{i(\boldsymbol{k}-\boldsymbol{k}'+\boldsymbol{q})\cdot\boldsymbol{R}_j} \frac{1}{N} \int_{cell} u^*_{\boldsymbol{k}'}(r) u_{\boldsymbol{k}}(r) e^{i(\boldsymbol{k}-\boldsymbol{k}'+\boldsymbol{q})\cdot\boldsymbol{r}} dr \tag{2.12}$$

It can be shown that the sum over j is equal to N when $\mathbf{k} - \mathbf{k}' + \mathbf{q} = \mathbf{G}$, where $\mathbf{G}$ is a vector of the reciprocal lattice, otherwise the sum is equal to zero (JACOBONI, 2010).

Using the results obtained above, the transition rate of the jth process from a state $|\mathbf{k}, \mathrm{c}\rangle$ to a state $|\mathbf{k}', \mathrm{c}'\rangle$ expressed in equation (2.8) can be rewritten as

$$\Gamma_j[\mathbf{k}, \mathbf{c}; \mathbf{k}', \mathbf{c}'] = \frac{2\pi}{\hbar} \left| \sum_q \langle c' | \mathcal{H}'_j(\mathbf{q}, \mathbf{y}) | c \rangle \right|^2 \mathcal{g} \delta(E(\mathbf{k}', c') - E(\mathbf{k}, c)) \tag{2.13}$$

Where $\mathcal{g}$ - which is called overlap equation – is given by

$$\mathcal{g} = \left| \int_{cell} u^*_{\boldsymbol{k}'}(\mathbf{r}) u_{\boldsymbol{k}}(\mathbf{r}) e^{i\boldsymbol{G}\cdot\boldsymbol{r}} d\mathbf{r} \right|^2 \tag{2.14}$$

The expression that calculates the total scattering rate of the jth scattering mechanism is achieved by integrating equation (2.13) over all available states $\mathbf{k}'$. The total scattering rate describes the probability of a charge carrier that is in a state $\mathbf{k}$ in a band n transits to any available state $\mathbf{k}'$ due a scattering event caused by the jth mechanism and is given by equation (2.15) (XIAOJIANG, 2000).

$$\Gamma_j(k) = \frac{V}{(2\pi)^3} \int_0^{2\pi} d\phi \int_0^{\pi} sin\theta d\theta \int_0^{\infty} \Gamma_j[\mathbf{k}, \mathbf{c}; \mathbf{k}', \mathbf{c}'] k'^2 dk' \tag{2.15}$$

It is important to notice that the Fermi's Golden rule has limitations. This rule is valid when the interactions are weak, which means, the scattering is infrequent, and the collision broadening can be neglected (VASILESKA; GOODNICK; KLIMECK, 2010).

3 ENSEMBLE MONTE CARLO SI, GE AND SIGE

3.1 Materials: Si, Ge and SiGe alloys

Silicon and germanium are completely miscible, which means they fully dissolve in each other at any concentration (CALLISTER, 2001). Thus, Si and Ge can form binary alloys of the type $Si_{1-x}Ge_x$ where the germanium content can vary from x equal to 0 up to x equal to 1. The SiGe alloys are also semiconductor materials. The addition of germanium in silicon generates a material with lower band gap and lower resistivity (GILLESPIE, 2009). Besides, the carrier mobility in these alloys is higher than in pure silicon.

SiGe has been studied to be used as the channel material of p-MOSFETs, where a hole-mobility enhancement in comparison with Si p-MOSFET has been found. This remark enables the use of these alloys when a device of high speed is expected (WHALL, 1998). Besides the higher mobility of holes, it has been shown that including SiGe layers between the insulator and the silicon substrate of a p-MOSFET results in a transistor that has superior reliability with respect to Negative Bias Temperature Instability.

Both silicon and germanium crystallize in a diamond lattice, however, the lattice parameter of silicon is 5.43Å while the lattice parameter of germanium is 5.65Å. In SiGe alloys, the atoms of Ge replace the Si atoms in the lattice, keeping the diamond lattice. In a random alloy such SiGe, the atoms are randomly distributed on the lattice. To describe the properties of random alloys, the Virtual Crystal Approach (VCA) is usually used. In this method, instead of considering that the constituent atoms of the alloy are randomly distributed, the crystal of the alloy is considered as the crystal of a "hybrid" atom, which is a combination of the constituent atoms. Figure 3.1 shows how the alloy lattice is depicted in the VCA, a hybrid atom represents the alloy instead of a crystal with Si and Ge atoms randomly distributed.

Figure 3.1 - Description of the virtual crystal approximation.

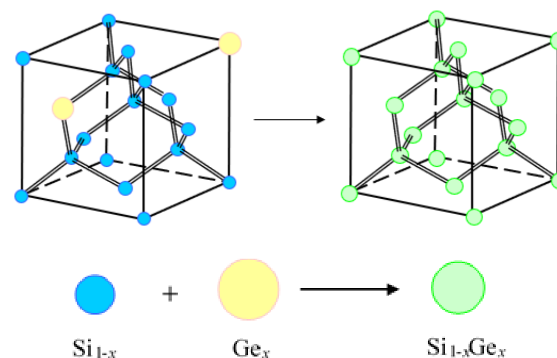

Source: Adapted from Gonzalez (2002).

Employing the VCA approach, the properties of SiGe alloy can be specified by linearly interpolating the properties of each atom in proportion to the respective content (GONZALEZ, 2001). Therefore, VCA model a crystal with physical parameters that vary between the physical parameters of the two pure crystals.

Since the interest of this work is simulating the transport of holes in Si, Ge and SiGe alloy, the band of interest is the valence band. Silicon and Germanium crystals - and their alloy - have similar valence structure, which is better described when heavy-hole, light-hole and split-off band are considered. The energy maxima of these three bands occur at gamma point. At this symmetry point, the heavy-hole and light-hole are degenerated, while the split-off band has a lower energy. The difference between the top of split-off band and the top of heavy and light hole band is caused by the spin-orbit interaction, it is called spin-orbit splitting energy and can be referred as Δ. The spin-orbit splitting energy of semiconductors is proportional to the fourth power of the atomic number of the element (KRISHNAN, 2005). For Silicon, Δ is equal to 0.044 eV, for germanium is 0.29 eV.

In the simulation of hole transport in the pure Si and Ge bulk, the most important scattering mechanism are caused by phonons. Nevertheless, when it comes to simulate the transport of holes in the SiGe alloys, the alloy scattering must also be included. To describe the phonon spectrum of the alloy, two approaches have been adopted, one considers an averaged spectrum and the other take into account the coexistence of both Si and Ge modes (BRIGGS; WALKER; HERBERT, 1998; FISCHETTI; LAUX, 1996). Using the same assumptions made by Briggs, Walker and Herbert (1998) and Fischetti and Laux (1996), in the simulation of hole transport in SiGe, the optical modes of pure Si and Ge coexist in the alloy and the acoustic branch is considered an average of the modes of pure Si and Ge.

3.2 Band Structure Model

To simulate the transport of hole in silicon, germanium and SiGe alloys, the valence band of these materials must be described in the transport code. The effective mass approach was used rather than employing a full band Monte Carlo simulation. The choice was made considering that if the full band structure methodology was used, the time of each transport simulation would increase due to the long time necessary to calculate the band structure and a large memory would be consumed due to the storage of the full k-dependent scattering rates.

Besides, it has been shown that satisfactory results are achieved when the effective mass approach - considering the nonparabolicity and warping effects- is employed to simulate hole transport in silicon (CAMARGO, 2016; DEWEY; OSMAN, 1993; RODRÍGUEZ-BOLÍVAR,

2005) and germanium (RODRÍGUEZ-BOLÍVAR, 2005). Therefore, including the nonparabolicity and warping effect to model the dispersion relation of light hole and heavy hole bands of silicon, germanium and SiGe alloys is adequate to simulate the transport of holes in these materials.

The split-off band is plausibly described as a spherical parabolic band; thus, its dispersion relation is given by equation (3.1)

$$E = \frac{\hbar^2 k^2}{2m_{so}} \tag{3.1}$$

Where m_{so} is the effective mass of split-off band.

However, heavy hole and light hole bands of both silicon and germanium are known for being warped and nonparabolic. Therefore, instead of poorly describe the effective mass using a unique value through all the Brillouin Zone, the nonparabolicity and warping effect must be taken into account. The methodologies to find an analytical expression that consider the impact of the warping and nonparabolicity on the dispersion relation are presented in the following sections.

3.2.1 Warping

The energy surface of a warped band is not spherically symmetric along the [100] and [111] directions. To describe the warping effect in the analytical equation of the dispersion relation, quadratic cross terms were considered by Dresselhaus (FERRY, 2013), which removes the spherical symmetry of the dispersion relation. The equation proposed by Dresselhaus, Kip and Kittel (1955) to take into account the warping effect in the heavy and light hole band is describe by

$$E(k) = \frac{\hbar^2}{2m_0}[\mathrm{A}k^2 \mp [\mathrm{B}^2 k^4 + \mathrm{C}^2\left(k_x^2 k_y^2 + k_y^2 k_z^2 + k_z^2 k_x^2\right)]^{1/2} \tag{3.2}$$

In equation (3.2), A, B and C are Dresselhaus parameters, m_0 is the mass of a free electron and the upper signal correspond to the expression of heavy hole and the lower signal correspond to light hole. The expression above can be rewritten in terms of the orientation of the wavevector:

$$E(k) = \frac{\hbar^2 k^2}{2m_0} |A|\left(1 \mp g(\theta, \phi)\right) \tag{3.3}$$

Where $g(\theta, \phi)$ is equal to

$$g(\theta, \phi) = \left[\left(\frac{B}{A}\right)^2 + \left(\frac{C}{A}\right)^2 (sin^4\theta cos^2\phi sin^2\phi + sin^2\theta cos^2\theta)\right]^{1/2} \tag{3.4}$$

The A, B and C parameters of Silicon and Germanium are well known. However, to describe the warping effect in heavy hole and light hole bands of SiGe alloys, these parameters must be determined for each alloy. The methodology used to achieve these parameters is based on calculating the band structure of each alloy and then extracting Dresselhaus parameters by a curve fitting process.

Firstly, the Empirical Pseudopotential Method code that was developed by Gonzalez (2001) was used to calculate the band structure of SiGe alloys from the gamma point, where the heavy and light hole band have their maxima, to both the directions [100] and [111] near the edge, where the nonparabolicity can be neglected. Next, the Dresselhaus parameters were extracted by fitting equation (3.3) to the values of energy and wavevector of heavy hole and light hole band calculated by EPM. Noticing that the constraint of the curve fitting process is that the best set of A, B and C parameters is the one that efficiently describe the warping of both heavy and light hole in both directions.

Figure 3.2 - Fit of the Dresselhaus, Kip and Kittel (1955) curve to the EPM band structure near the top of the heavy hole and light hole bands.

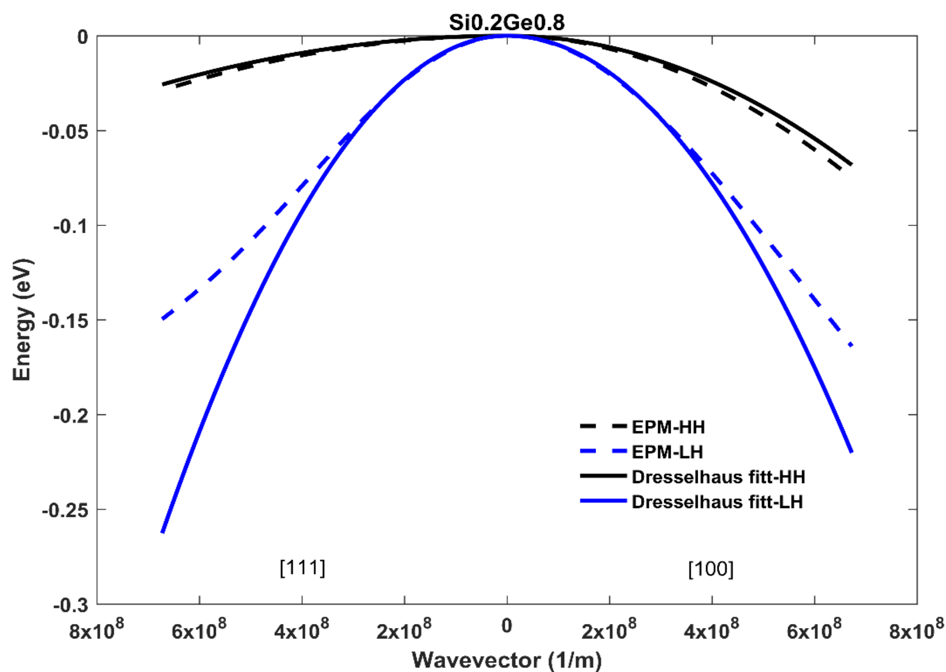

Source: author.

Figure 3.2 shows the heavy hole and light hole of the $Si_{0.2}Ge_{0.8}$ calculated by EPM and the fit of Dresselhaus, Kip and Kittel (1955) - equation (3.3) - to the EPM band structure. The left side of the graphic is band structure calculated in the [111] direction while the right side is the band structure calculated in the [100] direction. The blue curves are the light hole band and the black ones are the heavy hole band. Comparing the fitted curves with the EPM curves, it is possible to note a good level of agreement between them around the top of both bands.

3.2.2 Nonparabolicity

When the dispersion relation is expanded into Taylor series usually only the quadratic term is used to express the relation between energy and wavevector. However, sometimes the energy is badly described as a quadratic function of the wavevector. The nonparabolicity comes from the higher order terms of Taylor series expansion (MECHOLSKY et al., 2016).

Instead of expanding the dispersion relation into higher order terms, the nonparabolicity is taken into account by including a nonparabolicity factor into the expression of the dispersion relation. A nonparabolic band structure can be described by equation (3.5).

$$E(1 + \beta E) = \frac{\hbar^2 k^2}{2m^*} \tag{3.5}$$

Where m^* is the effective mass and β is the nonparabolicity factor. For silicon conduction band, the value of β is around 0.47, nevertheless, the nonparabolicity of the valence band of silicon, germanium and SiGe alloy is badly described by a constant.

Because of that, the nonparabolicity of the light hole and heavy hole band are usually described as a function of the energy (DEWEY; OSMAN, 1993; RODRÍGUEZ-BOLÍVAR; GÓMEZ-CAMPOS; CARCELLER, 2004). Dewey and Osman (1993) proposed that the nonparabolicity should be described as a quadratic function of the energy. Distinct parameters of the quadratic function were obtained for different ranges of energy for both light hole and heavy hole. His results show that the drift velocity for a large range of electric field coincides with the experimental data. However, the densities of states of both light hole and heavy hole band described by Dewey and Osman (1993) method have discontinuities, which is not physically accurate.

To overcome this issue, Rodríguez-Bolívar, Gómez-Campos e Carceller (2004) proposed describing the nonparabolicity factor of silicon and germanium using the analytical expression showed in equation (3.6).

$$\chi(E) = \frac{aE^2 + bE + c}{dE + 1} \tag{3.6}$$

In Rodríguez-Bolívar, Gómez-Campos e Carceller (2004) work, the band structure was estimated from gamma point to directions [111] and [100] using Kane method, then the nonparabolicity of the valence band was reached by fitting equation (3.6) to band structure data.

To fit the equation (3.6) to band structure data, Rodríguez-Bolívar, Gómez-Campos e Carceller (2004) divided the energy into small intervals in order to get the best set of parameters for each energy range. Rodríguez-Bolívar, Gómez-Campos e Carceller (2004) used this methodology to consider the nonparabolicity of both silicon and germanium, then simulated the drift velocity of both materials, obtaining results in good agreement with the experimental ones.

In this work, the nonparabolicity was considered by employing a similar methodology used by Rodríguez-Bolívar, Gómez-Campos e Carceller (2004). The new expression to dispersion relation of heavy hole and light hole band when both warping and nonparabolicity functions are included, are given in equation (3.7) and (3.8), respectively

$$E_H(k) = \frac{\hbar^2 k^2}{2m_0} |A|\big(1 - g(\theta,\phi)\big)\chi_H(E) \tag{3.7}$$

$$E_L(k) = \frac{\hbar^2 k^2}{2m_0} |A|\big(1 + g(\theta,\phi)\big)\chi_L(E) \tag{3.8}$$

Where $g(\theta,\phi)$ is given in equation (3.4) and $\chi_H(E)$ and $\chi_L(E)$ are the nonparabolicity functions of heavy hole and light hole, respectively. It is important to notice that each band has its own nonparabolicity function.

To find the nonparabolicity function $\chi(E)$ of each band of the material of interest, firstly, the Dresselhaus parameters were determined using the methodology described in the previous section. Secondly, the heavy hole and light hole bands were calculated again by the EPM method (GONZALEZ, 2001), however, in this case the entire bands were considered. The energy of the heavy hole and the light hole band are direction-depended, as the valence band of silicon shows in Figure 3.3. Therefore, the nonparabolicity is also direction dependent. To take it into account, the heavy and light band were calculated from gamma point to both [111] and [100] directions. To include all the valence band in the calculation, the top of the valence band up to -1eV was divided into a thousand of points for both directions.

Figure 3.3 – Silicon heavy and light hole band. In the left side of the graphic, these bands were calculated in the [111] direction and in the right side these bands were calculated in the [100] direction.

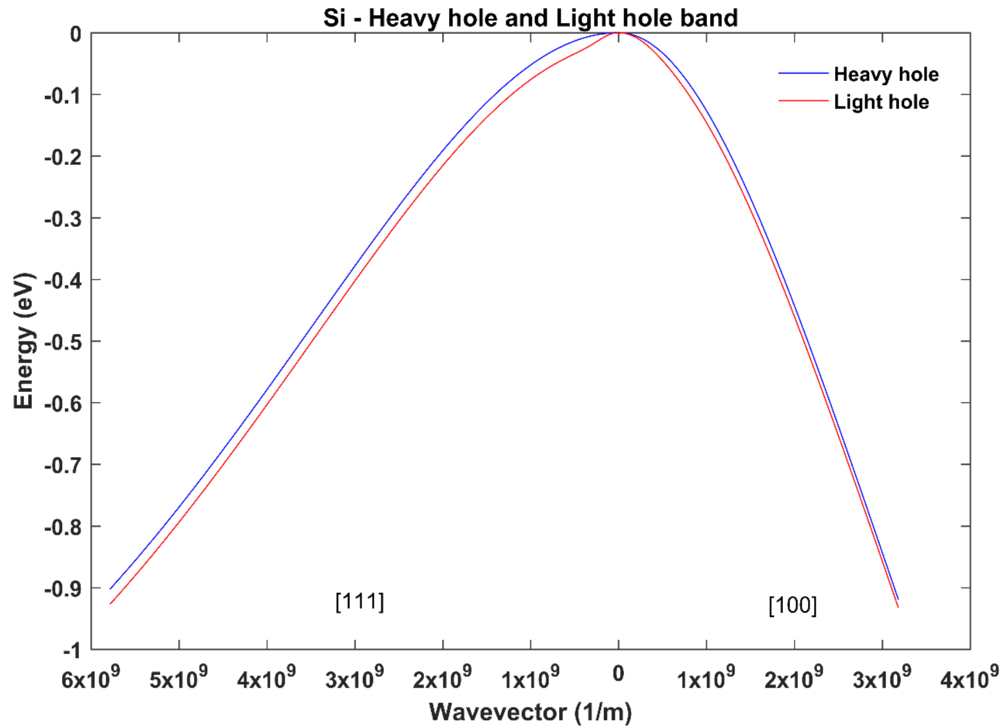

Source: Author

Having Dresselhaus parameters and the band structure data of heavy and light band in both directions, the nonparabolicity of both bands was calculated for each point in both directions by using equations (3.9) e (3.10).

$$\chi_H(E) = \frac{2m_0E(k)}{\hbar^2k^2|\mathrm{A}|\big(1 - g(\theta,\phi)\big)} \tag{3.9}$$

$$\chi_L(E) = \frac{2m_0E(k)}{\hbar^2k^2|\mathrm{A}|\big(1 + g(\theta,\phi)\big)} \tag{3.10}$$

Which resulted in a set of $\chi_{100}\big(E_{100}(\theta_{100},\phi_{100})\big)$ and $\chi_{111}\big(E_{111}(\theta_{111},\phi_{111})\big)$ for each band. Instead of having a nonparabolic function for each direction – which would increase the code complexity –, an average value of both energy and nonparabolicity was calculated at each point. Therefore, the direction dependency of the dispersion relation is concentrated only on the warping function. An averaged nonparabolic function was also employed by Rodríguez Bolívar, Gómez-Campos e Carceller (2004) in order to remove the direction dependence from it.

The analytical expression showed in equation (3.6) was fitted to the result data of E_{av} and χ_{av}, in order to obtain the parameters *a, b, c* and *d* of heavy hole and light hole band. To achieve plausible results, the energy range was divided into small intervals, then each interval has a set of parameters that best fit the nonparabolicity function. The parameters obtained by fitting were tested in two ways: First, when substituted in equations (3.7) and (3.8), these curves were compared with the band structure calculated using EPM code (GONZALEZ, 2001). Second, the result density of states must be physically acceptable. When one of those tests failed, the parameter was changed in order to accomplish both requirements. The constants *a, b, c and d* of light hole and heavy hole band of each material are given in the APPENDIX A of this work.

After employing this method, it was established - for each band - the analytical expression of nonparabolicity function. Substituting equation (3.6) into equation (3.7) and into equation (3.8), the final expression for the dispersion relation of heavy hole and light hole bands are given, respectively, by

$$E_H = \frac{(-bf_H k^2 + 1) - \sqrt{(bf_H k^2 - 1)^2 - 4(af_H k^2 - d)cf_H k^2}}{2(af_H k^2 - d)} \qquad (3.11)$$

$$E_L = \frac{(-bf_L k^2 + 1) - \sqrt{(bf_L k^2 - 1)^2 - 4(af_L k^2 - d)cf_L k^2}}{2(af_L k^2 - d)} \qquad (3.12)$$

Where f_H and f_L is the angular part of the dispersion relation of heavy hole and light hole band and are given by

$$f_H = \frac{\hbar^2}{2m_0} |A|\big(1 - g(\theta, \phi)\big) \qquad (3.13)$$

$$f_L = \frac{\hbar^2}{2m_0} |A|\big(1 + g(\theta, \phi)\big) \qquad (3.14)$$

In order to understand the importance of including the nonparabolic effect into the valence band of these material, the heavy hole band curve calculated by the analytical expression of equation (3.11) was compared with heavy hole band expression proposed by Dresselhaus, Kip and Kittel (1955). The heavy hole band of $Si_{0.2}Ge_{0.8}$ was calculated in both [111] and [100] directions employing these two methods. Figure 3.4 depicts these two curves

and the heavy hole dispersion relation calculated by EPM. Since the heavy hole band calculated by the EPM method can be considered the most accurate one, it is possible to note that the warped band overestimates the curvature of the heavy hole band in both directions, however this effect is more significant at [111] direction. The heavy hole band given by the analytical expression of equation (3.11) deviates less from the EPM band. This observation evinces the importance of including the nonparabolicity in the description of the valence bands of Si, Ge and SiGe alloys.

Figure 3.4 – Comparison between the heavy hole band of $Si_{0.2}Ge_{0.8}$ calculated by EPM, by the Dresselhaus, Kip and Kittel (1955) expression and by the analytical expression proposed by Rodríguez-Bolívar, Gómez-Campos e Carceller (2004)

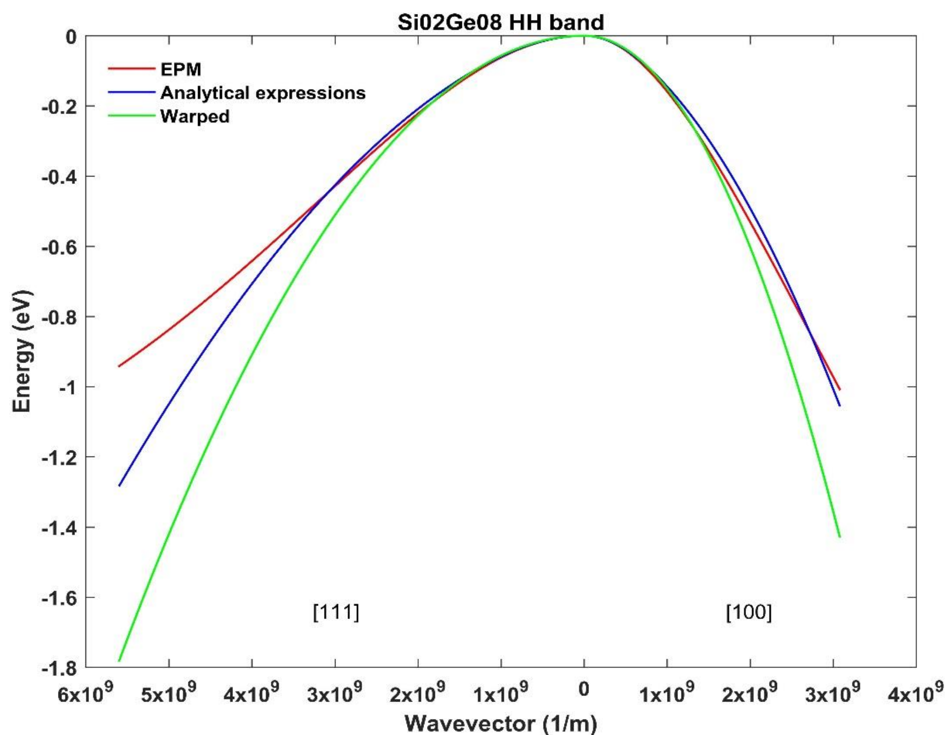

Source: Author

3.3 Scattering Rates

When simulating the transport of holes inside silicon and germanium bulk, the scattering mechanisms that play an important role are caused by acoustic and optical phonons. Since neither silicon nor germanium are polar materials, only nonpolar optical phonon scattering is present. When it comes to SiGe alloys, besides the ones already mentioned, a disorder scattering mechanism – called alloy scattering –, which is originated due to the random distribution of the silicon and germanium in the lattice, is also considered.

The interaction of each of those mechanisms with the charge carrier is described by a scattering potential, which represents the perturbation caused by the scattering process. For each scattering mechanism there is a transition rate, which describes the charge carrier transit probability from its $\mathbf{k}$ state in a band n to an empty state $\mathbf{k}'$ in a band m due the interaction. In the Ensemble Monte Carlo code, the scattering rates are stored as a function of the hole energy. The next sections present the scattering rate expressions as a function of the hole energy that are implemented in the simulation.

3.3.1 Acoustic Phonon Scattering Rate

Since the aim of this work is simulating the transport of holes in silicon, germanium and SiGe alloys materials, the approach presented here is used to calculate the hole scattering rate of acoustic phonons. In these materials, holes interact with phonons due to the deformation of the lattice which is generated by thermal vibrations (JACOBONI, 2010). In the deformation potential theory, the change in the energy of the charge carrier is related to the variation of the crystal volume (HAMAGUCHI, 2001). In the acoustic phonon scattering, the volume change is proportional the divergence of the displacement operator, $\mathbf{y}(\mathbf{r})$. Considering that, the perturbed Hamiltonian of acoustic phonon scattering is expressed as

$$H' = \sum_{ij} E_{ij} \frac{\partial y_i}{\partial r_j} \tag{3.15}$$

Where the i and j index correspond to the 3D axis of cartesian coordinate system. E_{ij} is the deformation-potential tensor and $\partial \mathrm{y}/\partial \mathrm{r}$ is divergence of the displacement operator, which express the deformation of the lattice caused by acoustic phonons. The displacement operator $\mathbf{y(r)}$ is given by equation (3.16) (JACOBONI, 2010).

$$\mathbf{y}(\mathbf{r}) = \sum_{\boldsymbol{q}} \mathbf{e}_{\boldsymbol{q}} \left(\frac{\hbar}{2\rho V \omega(\boldsymbol{q})}\right)^{\mathbf{1/2}} \{\mathrm{a}_{\boldsymbol{q}} + \mathrm{a}^{\dagger}_{\boldsymbol{-q}}\} e^{i\boldsymbol{qr}} \tag{3.16}$$

In this equation, $\mathbf{q}$ is the phonon wavevector, which is equal to $\mathbf{k} - \mathbf{k'}$, $\mathbf{e}_{\boldsymbol{q}}$ is the polarization vector of the acoustic phonon, V is the crystal volume and $\omega(\boldsymbol{q})$ is the angular frequency of the acoustic phonon, which is a function of the wavevector. In the equation (3.16), $\mathrm{a}_{\boldsymbol{q}}$ and $\mathrm{a}^{\dagger}_{\boldsymbol{-q}}$ are, respectively, the annihilation and creation phonon operators and ρ is the material

density. Substituting the expression of the displacement equation (3.16) into equation (3.15), the perturbed Hamiltonian becomes

$$H' = \sum_{ij} E_{ij} \sum_{\boldsymbol{q}} [\mathbf{e}_{\boldsymbol{q}}]\mathrm{i}\mathbf{q} \left(\frac{\hbar}{2\rho V\omega(\boldsymbol{q})}\right)^{\mathbf{1/2}} \{\mathrm{a}_{\boldsymbol{q}} + \mathrm{a}^{\dagger}_{-\boldsymbol{q}}\} e^{\boldsymbol{iqr}} \tag{3.17}$$

Since the expression of transition rate is given by

$$\Gamma[\mathbf{k}, \mathbf{c}; \mathbf{k}', \mathbf{c}'] = \frac{2\pi}{\hbar} \left| \sum_{q} \langle c'|\mathcal{H}'(\mathbf{q}, \mathbf{y})|c\rangle \right|^2 g\delta(E(\mathbf{k}', c') - E(\mathbf{k}, c)) \tag{3.18}$$

To calculate the acoustic phonon transition rate, the matrix element $\langle c'|\mathcal{H}'(\mathbf{q}, \mathbf{y})|c\rangle$ must be obtained. Comparing equation (3.17) with equation (2.9), it is possible to conclude that both are Fourier series expansions, therefore, $\mathcal{H}'(\mathbf{q}, \mathbf{y})$ of the acoustic scattering is given by

$$\mathcal{H}'(\mathbf{q}, \mathbf{y}) = \sum_{ij} E_{ij} \sum_{\boldsymbol{q}} [\mathbf{e}_{\boldsymbol{q}}]\mathrm{i}\mathbf{q} \left(\frac{\hbar}{2\rho V\omega(\boldsymbol{q})}\right)^{\mathbf{1/2}} \{\mathrm{a}_{\boldsymbol{q}} + \mathrm{a}^{\dagger}_{-\boldsymbol{q}}\} \tag{3.19}$$

After substituting equation (3.19) into equation (3.18), the presence of the annihilation and creation operators in $\mathcal{H}'_j(\mathbf{q}, \mathbf{y})$ establishes that the sum over $\mathbf{q}$ in equation (3.18) is only different from zero when $\mathbf{q} = \mathbf{k}' - \mathbf{k} + \mathbf{G}$ and $\mathbf{q} = \mathbf{k} - \mathbf{k}' + \mathbf{G}$. They correspond to the emission and absorption, respectively, of a phonon with wavevector equal to $\mathbf{q}$. Therefore, the sum of matrix element is constituted by these two terms. For these two cases, the action of the creation and annihilation operators on the crystal eigenstate is given by equation (3.20) and equation (3.21), respectively.

$$\left|\langle c'|\mathrm{a}_{\boldsymbol{q}}|c\rangle\right|^2 = N_q \tag{3.20}$$

$$\left|\langle c'|\mathrm{a}^{\dagger}_{-\boldsymbol{q}}|c\rangle\right|^2 = N_q + 1 \tag{3.21}$$

Where N_q is the phonon number in the $|\mathrm{c}\rangle$ state.

After substituting the terms of the matrix element in the transition rate equation, it becomes

$$\Gamma[\mathbf{k}; \mathbf{k}'] = \frac{\pi}{V} \frac{1}{\rho\omega(\mathbf{q})} \begin{bmatrix} N_q \\ N_q + 1 \end{bmatrix} \left| \sum_{\boldsymbol{ij}} \boldsymbol{E}_{\boldsymbol{ij}} [\mathbf{e}_{\boldsymbol{q}}]\mathbf{q} \right|^2 g\delta(E_{\mathbf{k}'} - E_{\mathbf{k}} \mp \hbar\omega(\mathbf{q})) \tag{3.22}$$

Where the upper terms correspond to the transition rate due to the absorption of an acoustic phonon and the down terms correspond to the transition rate due to the emission of and acoustic phonon.

Since the polarization vector in equation (3.22) has the same direction as the deformation, the product between $\mathbf{e}_q$ and $\mathbf{q}$ is equal to $\mathbf{q}$ for longitudinal acoustic phonons and zero for transverse modes (JACOBONI, 1989). To obtain a simplified expression to the acoustic transition rate, some approximations are made.

Firstly, due to the symmetry of cubic crystal, the deformation-potential – which is a second-rank tensor – can be considered a scalar value (JACOBONI, 1989). In addition, the overlap function $\mathcal{g}$ can be incorporated into the deformation potential (JACOBONI, 1989), resulting in the acoustic coupling constant $\mathrm{E_{ac}}$.

Secondly, the acoustic scattering can be considered elastic, this means the scattered hole maintains its energy after the scattering event. In the elastic approach the acoustic phonon scattering causes only intraband transition. In this case, the wavevector of acoustic phonons are small, therefore, the linear part of the acoustic dispersion relation - the equation that express phonon frequency as a function of the phonon wavevector - can be used. Thus, the energy of the phonon is equal to $\hbar \mathrm{qv_s}$, being $\mathrm{v_s}$ the sound velocity of the material. During the scattering, both crystal-momentum and kinetic energy are conserved, the expression of crystal-momentum and energy conservations of a system composed by a hole whose effective mass is m* and an acoustic phonon whose wavevector is $\mathbf{q}$ is given by

$$\begin{cases} \frac{\hbar^2 \mathrm{k'}^2}{2\mathrm{m}^*} = \frac{\hbar^2 \mathrm{k}^2}{2\mathrm{m}^*} \pm \hbar \mathrm{qv_s} \\ \mathrm{k'} = \mathrm{k} \pm \mathrm{q} \end{cases} \tag{3.23}$$

The module of phonon wavevector, for absorption and emission, are obtained after combining these equations showed in equation (3.23). The absorption and emission phonon wavevector are, respectively, given by equation (3.24) and equation (3.25).

$$\mathrm{q} = 2k(-cos\theta \ + \mathrm{v_s/v}) \tag{3.24}$$

$$\mathrm{q} = 2\mathrm{k}(cos\theta \ - \mathrm{v_s/v}) \tag{3.25}$$

Where v is the hole velocity. The maximum value of q occurs when the acoustic phonon is absorbed, and the hole is backward scattered. Since the velocity of holes are greater than the

sound velocity, the term v_s/v is almost zero, thus, the maximum value of q is approximately 2k (JACOBONI, 2010). The corresponding maximum energy transferred to phonon is

$$\hbar q_{max} v_s \approx 2\hbar k v_s = 2m^* v v_s \tag{3.26}$$

Which is lower than hole kinetic energy. Therefore, Considering the acoustic scattering as elastic scattering is a reasonable approach when the transport simulation is made at room temperature (JACOBONI, 2010).

The third assumption concerns the phonon population. The phonon population in a state **q** is given by the Bose-Einstein distribution, demonstrated on equation (3.27).

$$N_q = \frac{1}{e^{\frac{\hbar q v_s}{K_B T}} - 1} \tag{3.27}$$

The phonon population expression can be approximated to equation (3.28) when the thermal energy is much higher than the phonon energy, which is reasonable for room temperatures.

$$N_q = \frac{k_B T}{\hbar q v_s} - \frac{1}{2} \tag{3.28}$$

Employing these three approximations above, the acoustic transition rate becomes

$$\Gamma[\mathbf{k};\mathbf{k}'] = \frac{\pi}{V} \frac{E_{ac}{}^2 q}{\rho v_s} \left[\frac{K_B T}{\hbar q v_s} \mp \frac{1}{2} \right] \delta(E_{\mathbf{k}'} - E_{\mathbf{k}}) \tag{3.29}$$

Where the upper and lower signs refer to absorption and emission of an acoustic phonon. Since in the elastic approximation there is no difference between the final state achieved by emission and by absorption processes, the transition rate of acoustic phonon can be rewritten as the sum of the transition rates of emission and absorption (JACOBONI, 2010). Equation (3.30) express the acoustic transition rate as a sum of acoustic transition rate due to phonon emission and absorption.

$$\Gamma[\mathbf{k};\mathbf{k}'] = \frac{2\pi E_{ac}{}^2 K_B T}{\hbar V \rho v_s{}^2} \delta(E_{\mathbf{k}'} - E_{\mathbf{k}}) \tag{3.30}$$

To achieve the total scattering rate out of a state **k**, an integration over all states **k'** must be made in equation (3.30), which yields in equation (3.31).

$$\Gamma(\mathbf{k}) = \frac{V}{(2\pi)^3}\int \frac{2\pi {E_{ac}}^2 K_B T}{\hbar V \rho {v_s}^2}\delta(E_{\mathbf{k'}} - E_{\mathbf{k}})d\mathbf{k}' \tag{3.31}$$

Where $d\mathbf{k}' = {k'}^2 sin\theta dk' d\theta d\phi$.

Since the scattering rate must be calculated as a function of hole energy, it is useful to change the variable from $\mathbf{k}'$ to E'. The relation between theses variables is obtained from the dispersion relation of the final band. Since the acoustic phonon is an intraband scattering, the initial band and the final band is the same after the scattering. In the previous section, the dispersion relation of heavy and light hole was described in terms of an effective mass that consider both nonparabolicity and warping effect, whereas the dispersion relation of split-off band was described as a spherical parabolic band. ${k'}^2 dk'$ for heavy hole, is given by equation (3.32), for light hole band is given by equation (3.33) and for split-off band is given by equation (3.34).

$$({k'}^2 dk')_H = \frac{(2m_0)^{3/2}}{2\hbar^3 |A|^{3/2}\left(1 - g(\theta,\phi)\right)^{3/2}} \frac{(dbE'^2 + 2dcE' - aE'^2 + c)E'^{1/2}(dE' + 1)^{1/2}}{(aE'^2 + bE' + c)^{5/2}} dE' \tag{3.32}$$

$$({k'}^2 dk')_L = \frac{(2m_0)^{3/2}}{2\hbar^3 |A|^{3/2}\left(1 + g(\theta,\phi)\right)^{3/2}} \frac{(dbE'^2 + 2dcE' - aE'^2 + c)E'^{1/2}(dE' + 1)^{1/2}}{(aE'^2 + bE' + c)^{5/2}} dE' \tag{3.33}$$

$$({k'}^2 dk')_{SO} = \frac{(2m_{so})^{3/2}}{2\hbar^3}\sqrt{E'}dE' \tag{3.34}$$

The total acoustic scattering rate for holes in heavy hole is obtained by substituting equation (3.32) in equation (3.31) and integrating over all energy levels, which results in

$$\Gamma(E) = \frac{\sqrt{2}E_{ac}^2 k_B T (m_0)^{3/2}}{4\pi^2 \rho v_s^2 \hbar^4 |A|^{3/2}} \frac{(dbE^2 + 2dcE - aE^2 + c)E^{1/2}(dE + 1)^{1/2}}{(aE^2 + bE + c)^{5/2}} \mathrm{I}_H \tag{3.35}$$

Where E is the hole energy and I_H is the heavy hole angular integral given by

$$\mathrm{I}_H = \int_0^{2\pi} d\phi \int_0^{\pi} \frac{1}{\left(1 - g(\theta,\phi)\right)^{3/2}} sin\theta d\theta \tag{3.36}$$

The total acoustic scattering rate for holes in light hole is obtained by substituting equation (3.33) in equation (3.31) and integrating over all energy levels, which is given by

$$\Gamma(E) = \frac{\sqrt{2}E_{ac}^2 k_B T (m_0)^{3/2}}{4\pi^2 \rho v_s^2 \hbar^4 |A|^{3/2}} \frac{(dbE^2 + 2dcE - aE^2 + c)E^{1/2}(dE+1)^{1/2}}{(aE^2 + bE + c)^{5/2}} \mathrm{I}_L \tag{3.37}$$

Where I_L is the light hole angular integral given by

$$\mathrm{I}_L = \int_0^{2\pi} d\phi \int_0^{\pi} \frac{1}{\left(1 + g(\theta,\phi)\right)^{3/2}} sin\theta d\theta \tag{3.38}$$

The total acoustic scattering rate for holes in split-off band is obtained by substituting equation (3.34) in equation (3.34) and integrating over all energy levels, which results in equation (3.39).

$$\Gamma(E) = \frac{\sqrt{2}E_{ac}^2 k_B T (m_{so})^{3/2}}{\pi \rho v_s^2 \hbar^4} \sqrt{E} \tag{3.39}$$

The acoustic deformation potential can be obtained experimentally, however, in transport simulation, a common procedure is adjusting the acoustic coupling constant value until achieving a drift velocity that agrees with experimental results (RODRÍGUEZ-BOLÍVAR et al., 2005).

3.3.2 Optical Phonon Scattering Rate

A similar methodology is used to calculate the nonpolar optical scattering rate. The interaction between holes and nonpolar optical phonons occurs because the energy felt by the hole is changed as a result of the displacement of atoms with respect their equilibrium position caused by optical phonons. Although acoustic and optical phonons generate a displacement of the atoms in the lattice, changing the volume of the crystal, the expression of the volume variation caused by acoustic and nonpolar optical are different, therefore, they present distinct perturbed Hamiltonian (HATHWAR, 2011).

Acoustic phonons are caused by the oscillation of atoms in the same direction; therefore, the volume change is proportional to the divergence of the displacement operator. On the other hand, the optical phonons are caused by the oscillation of atoms in opposite directions, (SÓLYOM, 2007); therefore, the variation of volume is proportional to the displacement

operator. Thus, the perturbed Hamiltonian of the nonpolar optical phonon scattering, which is shown in equation (3.40), is proportional to displacement operator.

$$H' = D_{op}\mathbf{y}(\mathrm{r}) = \mathrm{D_{op}} \sum_{\mathrm{q}} \mathrm{e_q} \left(\frac{\hbar}{2\rho V\omega(\mathbf{q})}\right)^{1/2} \{\mathrm{a_q} + \mathrm{a}^{\dagger}_{-\mathrm{q}}\}\, \mathrm{e^{iqr}} \tag{3.40}$$

Where $\mathrm{D_{op}}$ is the optical deformation potential, which is second rank tensor, but can be considered a constant and $\mathbf{y}(\mathrm{r})$ is the displacement operator, given by equation (3.16). The Fourier coefficients of the nonpolar optical phonons, $\mathcal{H}_j'(\mathbf{q},\mathbf{y})$, is given by

$$\mathcal{H}'(\mathbf{q},\mathbf{y}) = D_{op} \sum_{\boldsymbol{q}} \mathbf{e}_{\boldsymbol{q}} \left(\frac{\hbar}{2\rho V\omega(\mathbf{q})}\right)^{\mathbf{1/2}} \{\mathrm{a}_{\mathbf{q}} + \mathrm{a}^{\dagger}_{-\mathbf{q}}\} \tag{3.41}$$

Again, the presence of the annihilation and creation operators in $\mathcal{H}_j'(\mathbf{q},\mathbf{y})$ impose that the sum over **q** in the matrix element in the expression of the transition rate, given by equation (3.18) is only different from zero when $\mathbf{q} = \mathbf{k}' - \mathbf{k} + \mathbf{G}$ and $\mathbf{q} = \mathbf{k} - \mathbf{k}' + \mathbf{G}$. Where **G** is a vector of the reciprocal lattice. First case corresponds to emission of a nonpolar optical phonon with wavevector equal to **q** and the second case corresponds to absorption of a nonpolar optical phonon with wavevector equal to **q.**

In these two cases, the matrix element results in N_q (absorption) and $N_q + 1$ (emission), where N_q is the optical phonon population. Since the dispersion relation of optical phonons are not dependent on the phonon wavevector (SÓLYOM, 2007), $\omega(\mathbf{q})$ is in fact a constant ω_{op} that assumes a different value for each material. In this case N_q is given by

$$N_q = \frac{1}{e^{\frac{\hbar\omega}{k_B T}} - 1} \tag{3.42}$$

Inserting the result of the matrix element into equation (3.18) and considering that both intraband and interband transitions can occur, the transition rate out of state **k** to any available state **k'** is given by

$$\Gamma[\mathbf{k};\mathbf{k}'] = \frac{\pi}{V}\frac{1}{\rho\omega_{op}} \begin{bmatrix} N_q \\ N_q + 1 \end{bmatrix} |D_{op}|^2 g\delta(E_{\mathbf{k}'} - E_{\mathbf{k}} \mp \hbar\omega_{op} + \Delta) \tag{3.43}$$

Where the upper terms correspond to the transition rate due to the absorption of an optical phonon and the down terms correspond to the transition rate due to the emission of and optical phonon. In the delta function in equation (3.43), $\hbar\omega_q$ is the energy of the phonon and Δ is the difference between the energies of the top of the final band and initial band.

The optical deformation potential constant D_{op} and the overlap integral $\mathcal{g}$ can be coupled to form the optical coupling constant, resulting in equation (3.44).

$$\Gamma[\mathbf{k};\mathbf{k}'] = \frac{\pi}{V}\frac{1}{\rho\omega_{op}}\begin{bmatrix} N_q \\ N_q+1 \end{bmatrix} D_{op}^2 \delta(E_{\mathbf{k}'} - E_{\mathbf{k}} \mp \hbar\omega + \Delta) \tag{3.44}$$

To find the total scattering rate out of a state **k**, an integration over all states **k'** must be made in equation (3.44), which becomes

$$\Gamma(\mathbf{k}) = \frac{V}{(2\pi)^3}\int \frac{\pi}{V}\frac{1}{\rho\omega_{op}}\begin{bmatrix} N_q \\ N_q+1 \end{bmatrix} D_{op}^2 \delta(E_{\mathbf{k}'} - E_{\mathbf{k}} \mp \hbar\omega + \Delta) d\mathbf{k}' \tag{3.45}$$

Where $d\mathbf{k}' = k'^2 sin\theta dk' d\theta d\phi$. To obtain the total scattering rate as a function of the energy, a variable change from **k'** to E' must be made in equation (3.45). Since the optical scattering assumes both intraband and interband transitions, it is important to notice that $E'(\mathbf{k})$ is the dispersion relation of the final band. If the final band is heavy hole, $k'^2 dk'$ is given by equation (3.32), if the final band is the light hole, $k'^2 dk'$ is given by equation (3.33), if the final band is split-off then equation (3.34) must be used.

To find the total nonpolar optical scattering rate out of heavy hole, light hole and split-off band to heavy hole, equation (3.32) is substituted into equation (3.45). After making the variable change and integrating over all the energy levels available, the expression for the total optical scattering is given by

$$\Gamma(E) = \frac{\sqrt{2} D_{op}^2 (m_0)^{3/2} N_{op}}{8\pi^2 \hbar^3 \omega_{op} |A|^{3/2}} \frac{(dbE'^2 + 2dc \mp \hbar\omega(E' - aE'^2 + c)E'^{1/2}(E'd+1)^{1/2}}{(aE'^2 + bE' + c)^{5/2}} \mathrm{I_H} \tag{3.46}$$

In equation (3.46), $\mathrm{I_H}$ is the heavy hole integral and is given by equation (3.36).

In equation (3.46), N_{op} is the phonon population and E' is the hole final energy. It is important to notice that the expressions of the hole final energy and the phonon population due to emission of an optical phonon are different from the ones due to absorption of an optical phonon. Therefore, the scattering rates are calculated separately by substituting these expressions for each case. The phonon population, referred in equation as N_{op}, is equal to $N_{op} =$

N_q when a phonon is absorbed and is equal to $N_{op} = N_q + 1$ when a phonon is emitted. The energy of the hole after absorption is given by $E' = E + \hbar\omega_q - \Delta$, where E is the energy of the hole before the scattering, and the energy of the hole after emission is given by $E' = E - \hbar\omega_q - \Delta$.

The total nonpolar optical scattering rate out of heavy hole, light hole and split of band to light hole band, is given by

$$\Gamma(E) = \frac{\sqrt{2}D_{op}^2(m_0)^{3/2}N_{op}}{8\pi^2\hbar^3\omega_{op}|A|^{3/2}} \frac{(dbE'^2 + 2dcE' - aE'^2 + c)E'^{1/2}(E'd + 1)^{1/2}}{(aE'^2 + bE' + c)^{5/2}} \mathrm{I_L} \tag{3.47}$$

In equation (3.47), $\mathrm{I_L}$ is the light hole integral and is given by equation (3.38).

The total nonpolar optical scattering rate out of heavy hole, light hole and split-off band to split-off band, is given by

$$\Gamma(E) = \frac{\sqrt{2}D_{op}^2(m_{so})^{3/2}N_{op}}{2\pi\hbar^3\omega_{op}} \sqrt{E'} \tag{3.48}$$

D_{op} is adjusted in order to obtain drift velocity data that agree with experimental results.

3.3.3 Alloy Scattering Rate

Although the Virtual Crystal Approach models the alloy crystal as a homogenous structure, in the real alloy there is a variation in the composition of the alloy related with the random distribution of the atoms. The random distribution of the atoms that constitute the alloy cause a disorder in the lattice, which generates a perturbation felt by the charge carrier while moving inside the alloy. Therefore, the perturbation comes from the disorder of the lattice and causes a variation in the potential felt by the charge carrier while moving.

The average potential felt by the charge carrier is given by equation (3.49) (HAMAGUCHI, 2001). Where V_a and V_b are the potential of the constituent atoms of the alloy A_xB_{1-x}.

$$V_0 = V_a x + V_b(1 - x) \tag{3.49}$$

Since the real alloy is not homogenous, there is a perturbation potential V' caused by the variation of the content, x', of the atoms in the lattice due to the random distribution of the atoms. The perturbed potential is given by (HAMAGUCHI, 2001)

$$V' = V_a x' + V_b(1 - x') \tag{3.50}$$

The alloy scattering potential can be expanded into a Fourier series, as shown in equation (3.51) (HAMAGUCHI, 2001).

$$V_{alloy}(\mathbf{r}) = \sum_{q} V_{alloy}(\mathbf{q}) e^{i\mathbf{q}\cdot\mathbf{r}} \tag{3.51}$$

Where the Fourier coefficient of the scattering potential $V_{alloy}(\mathbf{q})$ is independent of **q** and is given by the root-mean square of the difference between V' and V_0 (HAMAGUCHI, 2001), as equation (3.52) shows.

$$|\langle V' - V_0 \rangle| = |V_a - V_b| \left(\frac{x(1-x)}{N} \right)^{1/2} \tag{3.52}$$

In equation (3.52), N is the number of lattices. Substituting the scattering potential into the matrix element of the alloy scattering (HAMAGUCHI, 2001).

$$\langle \mathbf{k}' | H' | \mathbf{k} \rangle = |V_a - V_b| \left(\frac{x(1-x)}{N} \right)^{1/2} \delta(k' - k) \tag{3.53}$$

The transition rate expression for a transition from a state **k** to a state **k**′ is obtained by substituting the matrix element into equation (3.18), which results in

$$\Gamma[\mathbf{k}; \mathbf{k}'] = \frac{2\pi}{\hbar} |V_a - V_b|^2 \left(\frac{x(1-x)}{N} \right) \delta(E_{\mathbf{k}'} - E_{\mathbf{k}}) \tag{3.54}$$

To obtain the total scattering rate, equation (3.54) must be integrated over all **k’,** resulting in equation (3.55).

$$\Gamma(\mathbf{k}) = \frac{V}{(2\pi)^3} \int \frac{2\pi}{\hbar} |V_a - V_b|^2 \left(\frac{x(1-x)}{N} \right) \delta(E_{\mathbf{k}'} - E_{\mathbf{k}}) d\mathbf{k}' \tag{3.55}$$

In equation (3.55), V/N is the unit cell volume Ω_0.

The total alloy scattering rate is given by changing the variable of equation (3.55) the from $\mathbf{k}'$ to E', which was described in the previously sections, and integrating over all the energy levels. The total scattering rate for heavy hole, light hole and split-off band is given, respectively, by equations (3.56), (3.57) and (3.58).

$$\Gamma_H(E) = \frac{\Omega_0 (2m_0)^{3/2}}{8\pi^2\hbar^4} \Delta U^2 x(1-x) \frac{(dbE'^2 + 2dcE' - aE'^2 + c)E'^{1/2}(E'd+1)^{1/2}}{(aE'^2 + bE' + c)^{5/2}} \mathrm{I_H} \quad (3.56)$$

$$\Gamma_L(E) = \frac{\Omega_0 (2m_0)^{3/2}}{8\pi^2\hbar^4} \Delta U^2 x(1-x) \frac{(dbE'^2 + 2dcE' - aE'^2 + c)E'^{1/2}(E'd+1)^{1/2}}{(aE'^2 + bE' + c)^{5/2}} \mathrm{I}_L \quad (3.57)$$

$$\Gamma(E) = \frac{\Omega_0 (2m_{so})^{3/2}}{2\pi\hbar^4} \Delta U^2 x(1-x) \sqrt{E'} \quad (3.58)$$

Where E' is the hole energy after the scattering event.

The alloy potential scattering can be calculated or obtained experimentally. However, a common approach used in the simulation of charge carrier transport is finding a value for the potential scattering where the calculated mobility agrees with the experimental mobility.

3.4 Ensemble Monte Carlo code

To simulate the transport of charge carrier the Ensemble Monte Carlo method was chosen. The dispersion relation of valence band and the scattering rates are incorporated into the code. The heavy hole and light hole band are modeled as nonparabolic and warped, whereas the split-off band is described as parabolic and spherical. Only the phonon scattering rates described in the previously sections are included into the Si and Ge simulator. In the SiGe simulators, the alloy scattering plays an important role in the transport of holes in these alloys, considering that, besides the phonon scattering rates, the alloy scattering rate is also included.

The flowchart of the Ensemble Monte Carlo algorithm used in this work to simulate hole transport in silicon, germanium and SiGe alloys is depicted in Figure 3.5. In the following sections, each stage of the Monte Carlo algorithm presented in Figure 3.5 is described.

Firstly, the initialization process, which is composed by the routines “parameter initialization”, “scattering tables”, “carrier initialization” and “histograms”, is described. Here, the method employed to generate the free-flight times of each particle is demonstrated and the concept of scattering table is explained. In addition, how the algorithm uses these tables to select which scattering mechanism responsible for scattering the holes is explained.

Secondly, the routine that simulates the free-flight and the scattering events is specified. This section explains how the holes properties – velocity and energy – are updated in time, then describes the processes that involves the scattering event, which are choosing the scattering mechanism and updating energy and crystal wavevector of the scattered carrier.

Finally, the process used to acquire the data from the simulations, which in the flowchart showed in Figure 3.5 is called “writing data”, is explained.

Figure 3.5 - Flowchart of the main program for EMC simulation.

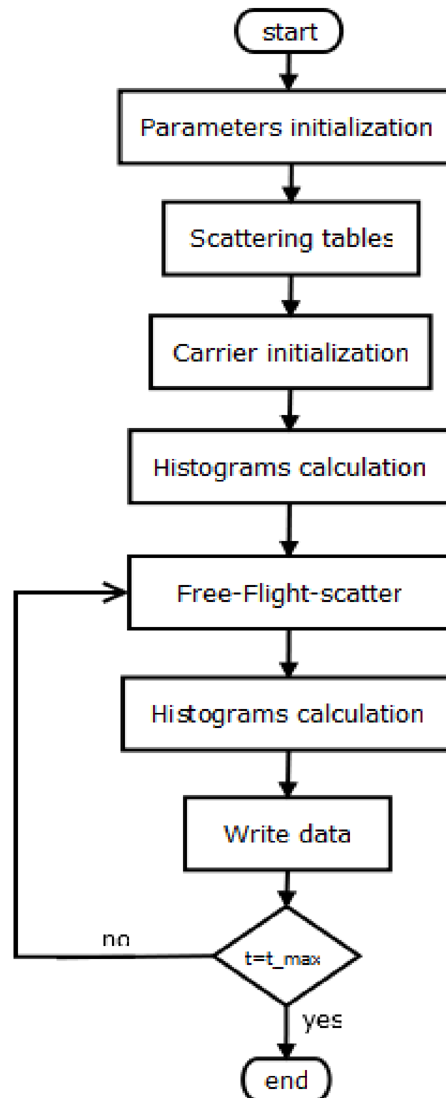

Source: Adapted from Vasileska, Goodnick and Klimeck, 2010.

3.4.1 Parameter Initialization

The flowchart in Figure 3.5 is initiated by the execution of the main routine. In the beginning of the simulation, before the time loop starts, it is necessary to assign values for external parameters which influence the charge carrier transport and parameters that describe the semiconductor. The main routine calls the *readin* subroutine where parameters such as number of carriers, temperature, electrical field, total time, observation time and effective mass are defined. In this routine the angular integrals of both heavy and light hole are calculated. In

the beginning of the simulation, besides assigning values to each parameter, scattering tables for each available band must be calculated.

3.4.2 Creating Scattering Tables

In the Monte Carlo simulation, after the free-flight time ends, a scattering even must occur. For each scattering mechanism, the total scattering rate of the hole should be evaluated in order to define which mechanism is more likely to scatter the particle. Calculating the scattering rate for each of the N mechanisms at all final free-flight period would highly spend computational time (VASILESKA; GOODNICK; KLIMECK, 2010). To avoid this, in the beginning of the simulation, for each available band, the scattering rate of each mechanism is calculated as a function of the carrier energy. This information is stored in a table, called scattering table, where the scattering rate is calculated for a large range of energy, so no carrier will reach an energy beyond the energy range covered by the table (CAMARGO, 2016). The equations that describe the scattering rate of each mechanism, which were demonstrated in the last section, are solved analytically in the code, in order to create the scattering table for all the three valence bands.

The process of creating a scattering table for each band is executed by the *scattering_table* subroutine. The first column of the scattering table contains the charge carrier energy, the second column contains the scattering rate of the 1st scattering mechanism for the entire energy range, the third column contains the sum of the scattering rate of the 1st and 2nd mechanism, the fourth column contains the sum of the scattering rate of the 1st, 2nd and 3rd mechanism, it goes on until the $N + 1$ column, which contains the summation of the scattering rates of all mechanism. Thus, a band that has N possible scattering mechanism has a table with $N + 1$ column. In the end, the scattering table of each band is normalized by its largest value, which is called Γ_0. The value of Γ_0 is used again in the generation of free-flight times described in section 3.4.5.

3.4.3 Carrier Initialization and Histograms Calculation

After the scattering tables are constructed, the carrier initialization is performed. Calling the *init* routine, each charge carrier is initialized with an energy, wavevector and with an initial free-flight time. The method utilized to generate free-flight time is depicted in section 3.4.4. In addition, in this stage, the code defines that initially all holes occupy the heavy hole band.

The initial energy of the ensemble is given by the Boltzmann distribution. In order to randomize the initial energy of the charge carrier, the initial energy is calculated by

$$E = -\frac{3}{2} k_B T \ln(rand1) \quad (3.59)$$

Where *rand1* is a random number uniformly distributed between 0 and 1.

The magnitude of the initial wavevector is related to the initial energy assigned to the hole, thus it is calculated using the dispersion relation of the hole band. The orientation of the wavevector is randomly assigned to the carrier, following the equations.

$$\phi = 2\pi rand2 \quad (3.60)$$

$$cos\theta = 1 - 2rand3 \quad (3.61)$$

In the equation (3.60), *rand2* is a random number uniformly distributed between 0 and 1 and ϕ is the azimuthal angle which can vary from 0 to 2π. In the equation (3.61), *rand3* is also a random number uniformly distributed between 0 and 1 and θ is the polar angle which can vary from 0 to π. After calculating the magnitude and the orientation of the wavevector, its components k_x, k_y and k_z can be calculated.

In order to ensure that energy and wavevector of charge carriers follow a Maxwell-Boltzmann distribution the histogram of energy and wavevector are calculated by calling the *histogram* subroutine. During the simulation, it is possible to call the *histogram* subroutine at each observation time in order to acquire energy and wavevector distribution in the entire simulation.

3.4.4 Generating Free Flight Time

In the Monte Carlo simulation, the charge carrier is said to have a free flight during the time between two successive scatterings (t_r). In order to simulate this process, the free-flight time – which is a random variable since the scattering events are stochastics – should be known. The free-flight time can be described in terms of the probability density, $P(t)$, where $P(t)dt$ is the probability that a charge carrier, after being scattered at time $t = 0$, will not be scattered at the interval of time t and then will suffer a scattering in time dt around t (VASILESKA; GOODNICK; KLIMECK, 2010).

The probability that a charge carrier will be scattered from a state $\mathbf{k}$ to a state $\mathbf{k}'$ at the time dt after having a free-flight period equal to t can be described in terms of the total scattering rate, $\Gamma[\mathbf{k}(t)]$ which is the sum of the contributions from each scattering mechanism. Being $\Gamma[\mathbf{k}(t)]dt$ the probability that a charge carrier will be scattered at time dt, then $\exp\left(-\int_0^t \Gamma[\mathbf{k}(t')]dt'\right)$ is the probability that a charge carrier will not suffer a scattering until time t (VASILESKA; GOODNICK; KLIMECK, 2010). Therefore, the probability that a charge carrier will scatter between t and $t + dt$, after having a free-flight equal to t, is given by the equation (3.62).

$$P(t)dt = \Gamma[\mathbf{k}(t)]\exp\left[-\int_0^t \Gamma[\mathbf{k}(t')]dt'\right]dt \tag{3.62}$$

To determine the free-flight time, (t_r), a methodology to obtain $P(t)$ in equation (3.62) is required. Thus, a random number generator which generates a uniformly distributed number r between 0 to 1 must be used. The equation (3.63) shows how r and $P(t)$ are related (LUNDSTROM, 2000).

$$r = \int_0^{t_r} P(t)dt \tag{3.63}$$

Integrating equation (3.63) after substituting the value of $P(t)$ given by equation (3.62) on equation (3.63) yields equation (3.64)

$$r = 1 - exp\left[-\int_0^{t_r} \Gamma[\mathbf{k}(t')]dt'\right] \tag{3.64}$$

Equation (3.64) can be rewritten substituting the term $1 - r$ for r, since they are statistically the same, in order to achieve equation (3.65).

$$\ln(r) = \int_0^{t_r} \Gamma[\mathbf{k}(t')]dt' \tag{3.65}$$

Solving the equation (3.65) to generate free-flight times for each charge carrier would spend a substantial amount of computational time (JACOBONI; LUGLI, 1989). Thus, to avoid the complexity of equation (3.65), an approach that makes the time dependence of the scattering rate vanish is required. This simplification is obtained by introducing the so-called self-

scattering method, which inserts a fictitious scattering process whose scattering rate is always adjusting itself in order to make the total scattering rate constant with respect to time (VASILESKA; GOODNICK; KLIMECK, 2010; JACOBONI; LUGLI, 1989). Thus, the scattering rate is defined as a sum of the real scattering rate and the self-scattering rate, as depicted in equation (3.66).

$$\Gamma_0 = \Gamma[\mathbf{k}(t)] + \Gamma_{self}[\mathbf{k}(t)] \tag{3.66}$$

This fabricated scattering process is defined as the scattering that provoke no changes in the charge carrier state nor on its trajectory. Thus, when this mechanism is selected to terminate the free flight, it has no effect on the free flight.

Employing this approach, the free-flight time can be written as

$$t_r = -\frac{1}{\Gamma_0}\ln(rand4) \tag{3.67}$$

Where the Γ_0 in equation (3.67) is defined in the beginning of the simulation and $rand4$ is a random number generated in the simulation.

3.4.5 Free-flight and Scattering

In the *free-flight-scatter* routine the charge carrier transport is simulated. The time in the simulation is discretized in time steps, Δt, where the motion of each charge carrier is independently simulated. To simulate the free flight, the *drift* subroutine is called, where charge carriers are freely accelerated by the electrical field. Whereas, when the free flight is terminated, a scattering event is simulated by the *scatter_carrier* subroutine.

The flowchart of the *free-flight-scatter* routine used to perform the hole movement during a time step, Δt, is depicted in Figure 3.6. The free-flight time, dte, of each particle must be evaluated at each observation time to decide whether the particle will keep the free flight or will be scattered. If dte is greater than Δt, no scattering happens in that time step; therefore, the particle freely moves during all the observation time and its free-flight time is decreased by Δt. On the other hand, if dte is smaller than Δt, it means the free flight must occur until dte, and then a scattering event must take place. The the mechanism that will scatter the particle at dte is defined at the *scatter_carrier* subroutine.

After the scattering mechanism is chosen, a new free-flight time $dt3$ is generated, for the recently scattered particle, in accordance with the method presented in section 4.2.1; if the free-flight time $dt3$ is smaller than the time left until the next observation time, dtp, the particle will freely move until the end of $dt3$.

On the other hand, if $dt3$ is greater than dtp the particle will freely move during dtp. Then, the free-flight time in this observation time is updated by summing dte and the new free-flight time $dt3$. If this sum is smaller than Δt, another scattering must occur before the next time step; therefore, another scattering mechanism must be selected, and a new free-flight time have to be randomly chosen. If this sum is greater than Δt, then the remainder free-flight time left is calculated by decreasing Δt.

Figure 3.6 - Flowchart of free_flight_scatter routine.

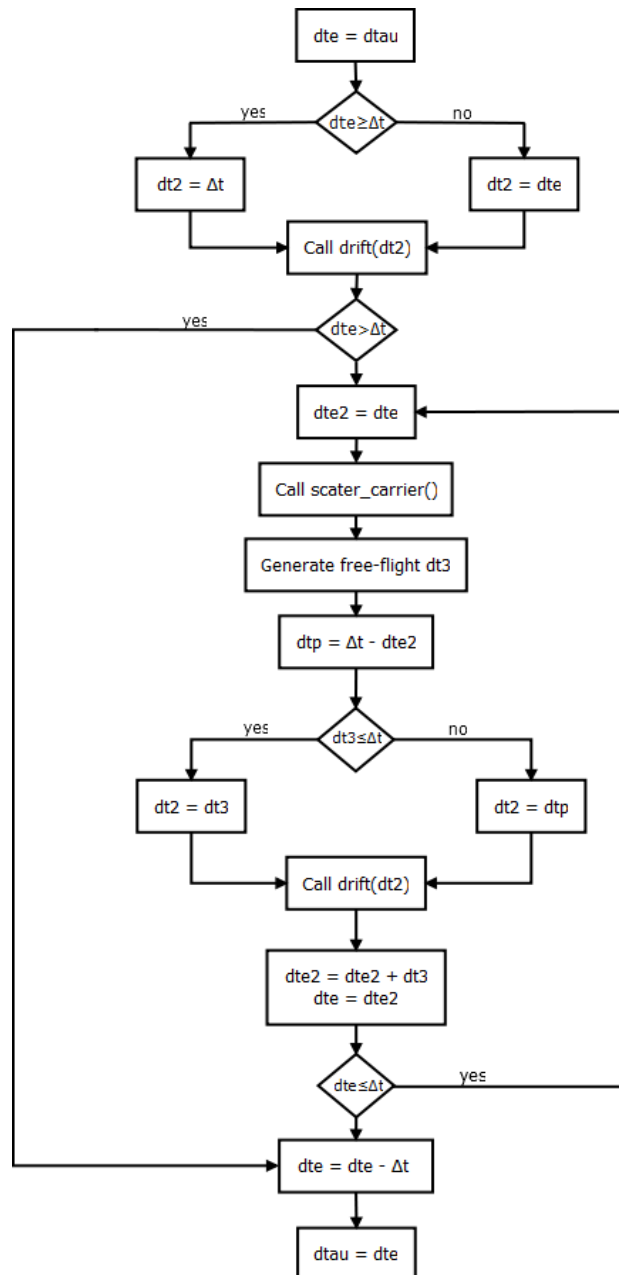

Source: Adapted from Vasileska, Goodnick and Klimeck, 2010.

In the subroutine *drift*, where the free-flight motion is performed, the crystal wavevector of every charge carrier is updated at each time step, according to the equation (2.3). During the time of free movement, the charge crystal wavevector of each carrier is changed only by the effect of electromagnetic field. Since the wavevector is changed due the drift movement, a new energy of the hole must be calculated based on the band the hole is occupying. If the hole is in the split-off band, equation (3.1) is employed to calculate the current energy, if the hole is in the heavy hole band, the equation (3.11) is used and if the hole is in the light hole band, equation (3.12) must be employed.

The velocity of the charge carrier is also related with the wavevector and is calculated in accordance with equation (3.68) (VASILESKA; GOODNICK; KLIMECK, 2010).

$$\mathbf{v} = \frac{1}{\hbar}\nabla_{\mathbf{k}}E_{\mathbf{k}} \tag{3.68}$$

The scattering event is simulated in the *scatter_carrier* subroutine. The role of this code is, firstly, selecting the mechanism responsible for scattering the charge carrier as depicted in section 3.4.6, then performing the changes on the wavevector and on the energy of the charge carrier. When the acoustic scattering mechanism is chosen, the hole energy remains the same since this is an elastic scattering in this simulator. When the nonpolar phonon process is selected, the hole will change its energy. The new energy depends on the initial and final band and whether an optical phonon will be absorbed or emitted.

When it comes to update the hole wavevector of a hole that transits to split-off band, the module of this vector is calculated using the dispersion relation of the final band. In this band, all scattering processes considered in this model – acoustic phonon scattering, nonpolar optical phonon scattering and alloy scattering - are considered isotropic, which means the wavevector after the scattering event is equally likely to assume any orientation. Considering that, both polar and azimuthal are generated using random numbers.

In the heavy and light hole band, the final wavevector is randomly determined, which means both polar and azimuthal angles are also generated using random numbers, nevertheless, to assure the new wavevector respect the relation with the energy defined in equation (3.11) for the heavy and in equation (3.12) for light hole bands, the rejection technique is used to accept the new wavevector or reject it.

3.4.6 Choosing the Scattering Mechanism

When the free-flight period ends, a scattering must happen. Since there are several mechanisms and each of them has a different impact on charge carrier energy and wavevector (LUNDSTROM, 2000), the process responsible for scattering the charge carrier should be selected before calculating the final state of the particle. The scattering mechanism will be chosen based on the charge carrier band and energy after the free-flight time.

Using a uniformly distributed random number $rand5$ which varies between 0 and 1, the mechanism that will scatter the charge carrier in the band m with energy E_m can be stochastically chosen by comparing $rand5$ with the values on the scattering table of the band m for that specific charge carrier energy, E_m. Since the first column on the scattering table contains the energy, selecting process consists on finding the value on the first column that coincide with the charge carrier energy, then, comparing $rand5$ with the value on second column; if $rand5$ is smaller than it, the first mechanism is chosen. If $rand5$ is greater than that, then, $rand5$ is compared with the value on third column; if $rand5$ is smaller than the third column value, the second mechanism is chosen. If $rand5$ is greater than the third column value, the analysis goes on until a mechanism is selected. However, if $rand5$ is greater than the value on last column, the self-scattering is chosen. In the code, the self-scattering mechanism is always verified first, because this mechanism is the most probable to occur for low-energy particles (CAMARGO, 2016).

3.4.7 Writing Data

At each time step, the quantities relate to the charge carrier transport are calculated. The velocity, in the three dimensions, and the energy of each charge carrier is calculated. Then, for each band the average energy and the average velocity are estimated. Thus, the progress of those averages can be evaluated with respect to time. Furthermore, the band population is measured at each observation time by calculating the number of charge carrier in each band.

The ensemble averages of the quantity A at a time t can be obtained by summing the $A_i(t)$ over all the N charge carrier considered in the simulation – $A_i(t)$ is the value that the quantity A assumes for the ith charge carrier at the time t. The expression to calculate the ensemble average of A is given in equation (3.69) (JACOBONI; LUGLI, 1989).

$$\langle A \rangle = \frac{1}{N} \sum_{i=1}^{N} A_i(t) \tag{3.69}$$

4 RESULTS

4.1 Silicon Transport Simulations

A set of simulations was performed to determine the value of each deformation potential constant. To select these constants, the condition was achieving the steady-state hole velocities that agree with experimental results for a range of the electric field (JACOBONI, 1977). Since the elastic approximation is not valid at low temperatures, the simulations were performed at 300K. In the experiments and in the simulation, the electric field was applied parallel to the [100] direction and it was varied from 10^3 to 10^5V/cm. The total time of the simulation was equal to 10ps for low fields (smaller than 10^4 V/cm) and 5ps for higher fields. The time of simulation was higher for low fields due to the fluctuation observed in the hole velocity and energy. In each of these simulations, 20000 holes were considered in the ensemble.

Figure 4.1 – Comparison between the simulated drift velocity of holes in silicon with experimental data. Electric field applied parallel to [100] direction.

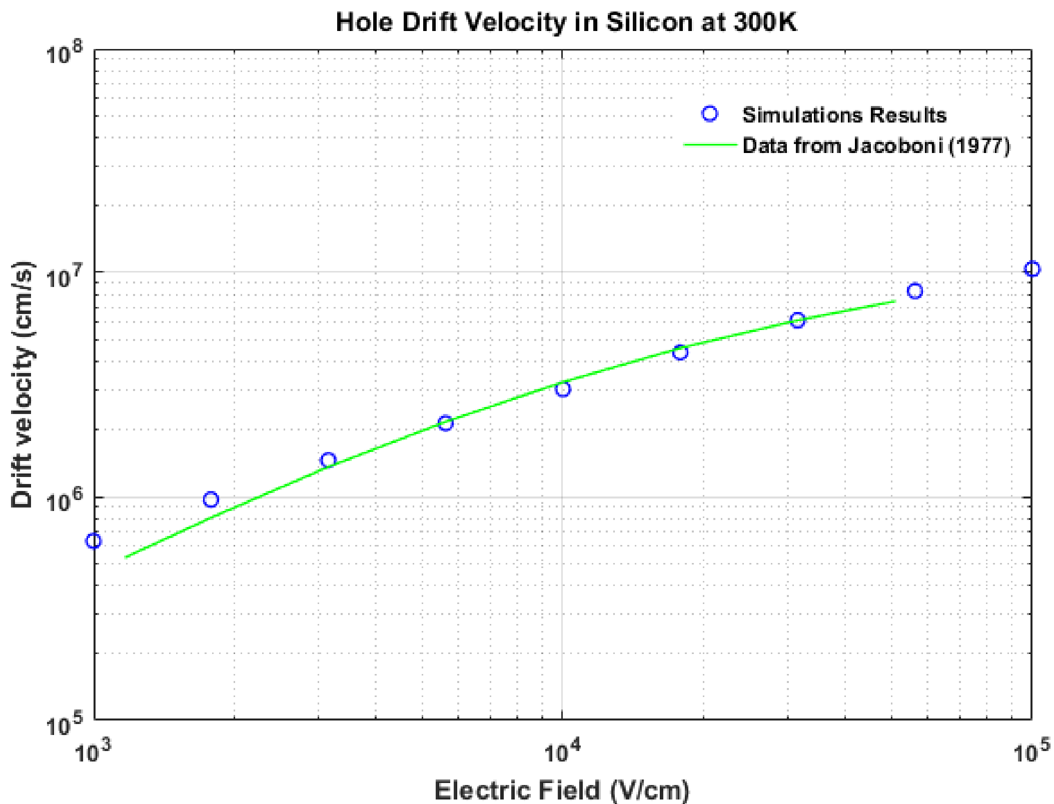

Source: author.

Figure 4.1 shows the results of the steady-state hole drift velocity as a function of the electric field obtained using the described simulator and experimentally (JACOBONI, 1977). As it is shown in the Figure 4.1, the simulated hole velocity is overestimated for low electric

fields in comparison with the experimental data, while is well described for electric fields higher than 1500V/cm. Good level of agreement between experimental and simulation data is observed.

Figure 4.2 shows the mean energy of holes for those simulations. For electric fields smaller than 10^4V/cm, the mean energy slowly rises with the increase of the electric field. As can be seen in Figure 4.2, electric fields from 10^4 to 10^5V/cm expressively increase the hole mean energy in silicon.

Figure 4.2 - Mean energy of the holes versus electric field for silicon bulk at 300K.

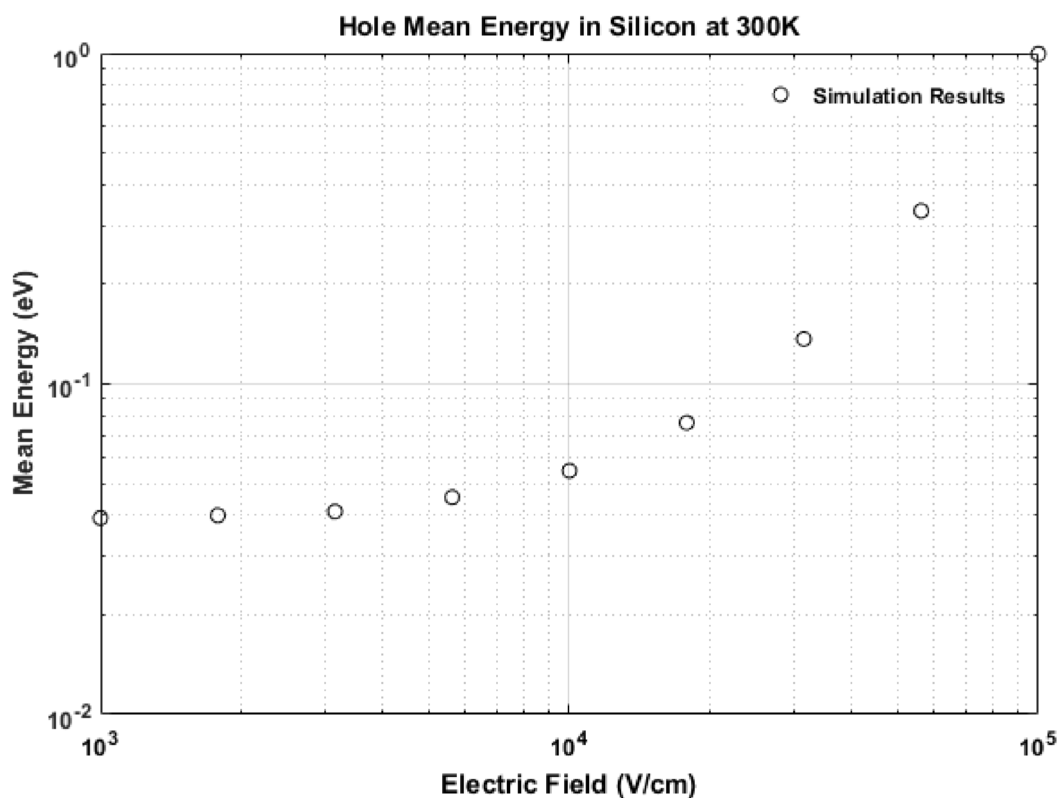

Source: author.

The graphic on Figure 4.3 shows the band occupancy as a function of the applied electric field. In the code, initially, all the holes are in the heavy hole band. Light hole and split off band eventually become occupied due to interband scattering process, which, in this model, are only caused by nonpolar optical phonon. Increasing the electric field generates a rise in the light hole population, which is accompanied by a decrease in heavy hole band population.

Figure 4.3 – Occupation of the valence bands vs electric field for Si at 300K.

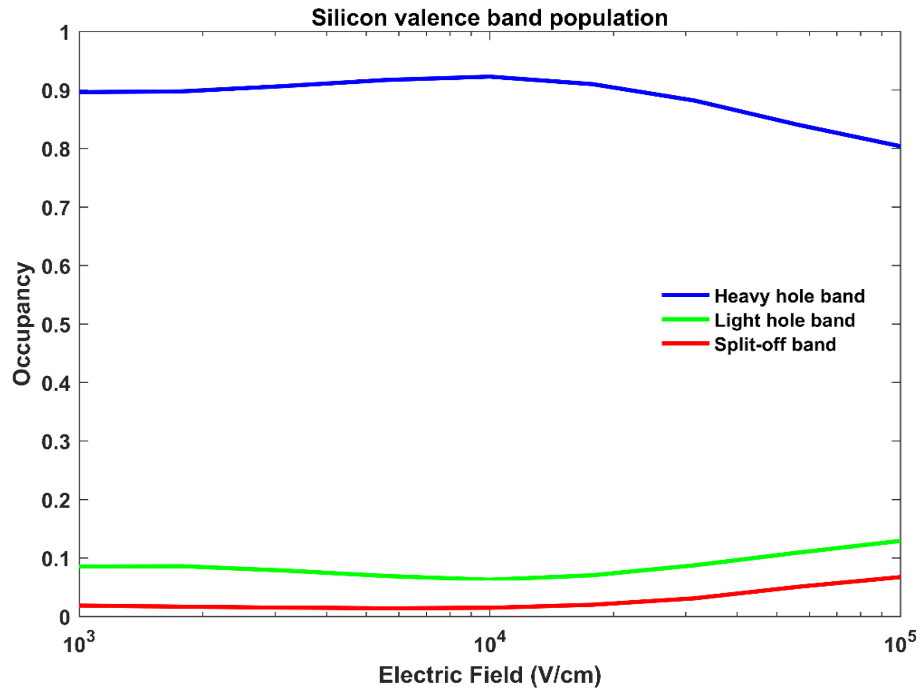

Source: Author

Other simulations of hole transport inside silicon bulk were performed at 300K to describe the time evolution of the drift velocity and of the energy of holes in silicon bulk. To obtain this relation, distinct simulations were performed where distinct electrical fields were applied only in the y-direction. Again, in each simulation, 20,000 holes were considered.

The time evolution of the energy of holes for electric fields of 15, 25, 50, 75 e 100 kV/cm is depicted in Figure 4.4. Those curves show that the charge carrier energy increases due to the external electrical field. The ensemble reaches a steady state when the increase in energy due to the electrical field is compensated by the loss of energy due to scattering events. The calculation of the energy, velocity and population at different values of electric field presented in Figure 4.2, Figure 4.1 and Figure 4.3 is only performed when the ensemble reaches the steady state.

Figure 4.5 shows the time evolution of the drift velocity of holes for electric fields of 15, 25, 50, 75 e 100 kV/cm. The velocity overshoot effect can be observed at the beginning of the simulation. The holes achieve a velocity higher than the expected because when the electric field is applied, it highly increases the charge carrier velocity. As the time goes, the scattering events decrease the charge carrier velocity and they also change the band population.

Figure 4.4 - Energy of holes in silicon for applied fields of 15, 25, 50, 75 and 100kV/cm

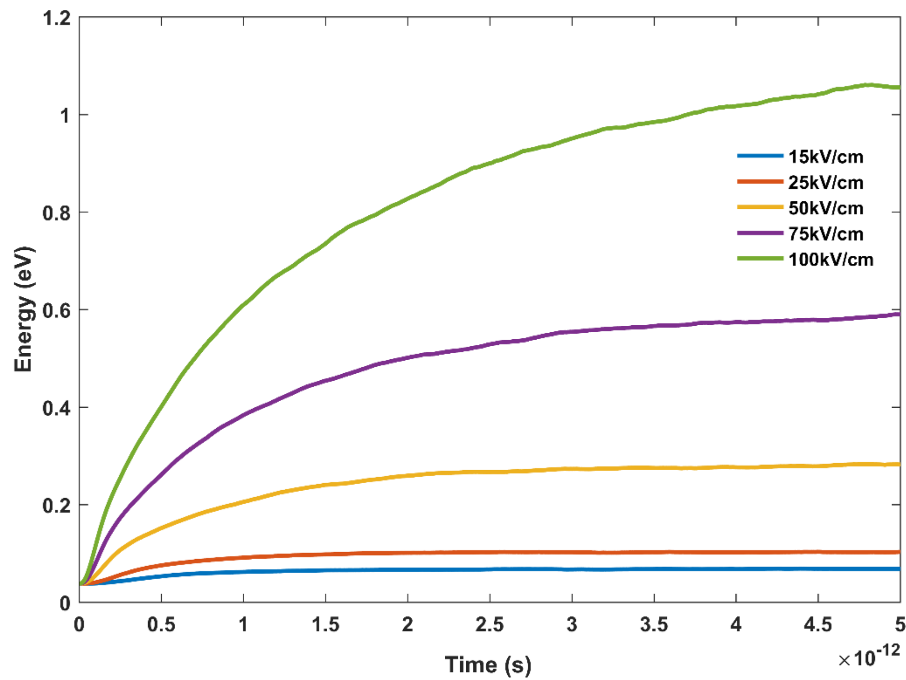

Source: author.

Figure 4.5 – Time evolution of drift velocity of holes in silicon for applied fields of 15, 25, 50, 75 and 100kV/cm. It is possible to observe the velocity overshoot and the steady state.

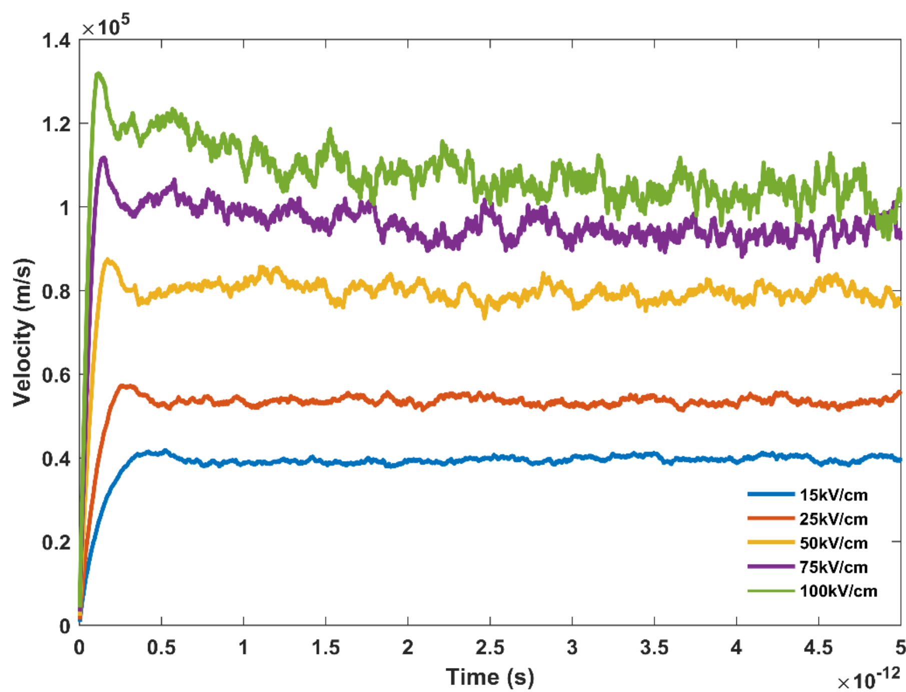

Source: Author

Figure 4.6 shows the intraband acoustic scattering rates for the three valence bands of silicon at 300K.

Figure 4.6 - Acoustic phonon scattering rates for holes in the heavy hole, light hole and split-off bands in Si. This scattering process is intra-band, which means the initial and the final bands are the same.

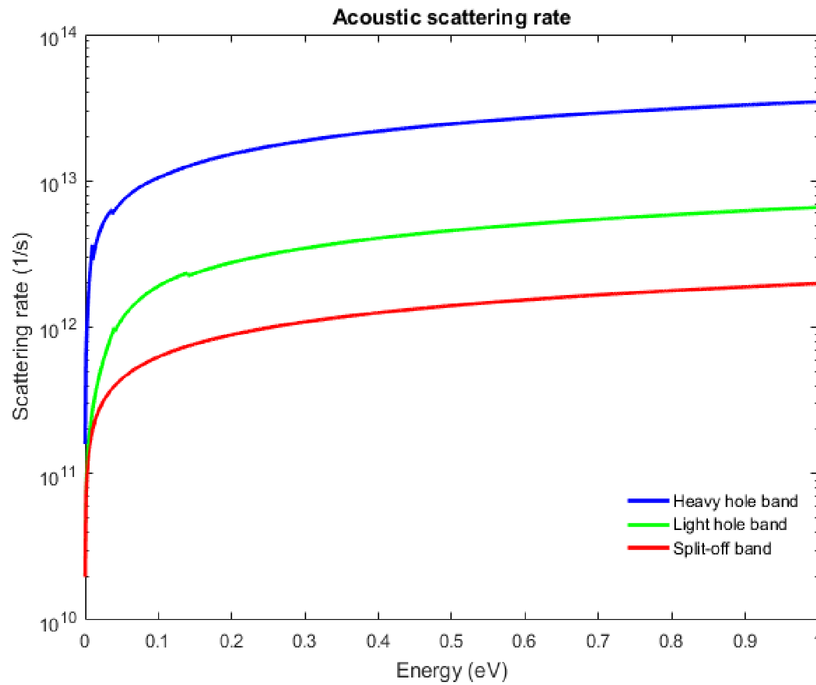

Source: Author

Figure 4.7 - Nonpolar optical phonon scattering rates for holes scattered from the heavy hole band in Si.

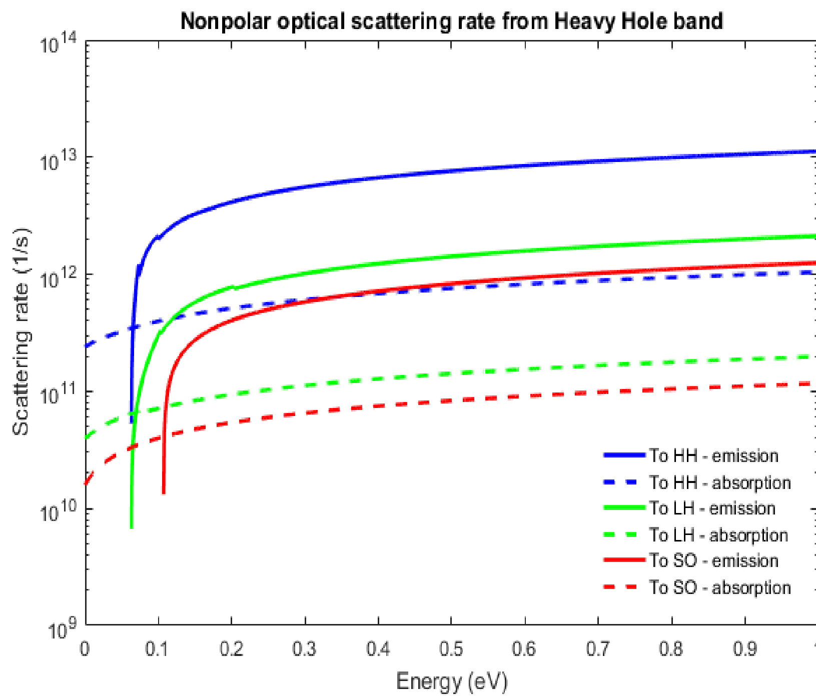

Source: Author

Figure 4.7 shows the optical scattering rates for holes that transit from heavy hole to heavy hole, light hole and split-off band. In silicon heavy hole band, the acoustic scattering rate

at 300K is greater than the nonpolar optical scattering, as can be seen comparing the blue curves in Figure 4.6 and in Figure 4.7. Therefore, the mobility of hole in this band is mainly restrained by the interaction of holes with acoustic phonons. As Figure 4.7 shows, the absorption of an optical phonon can occur at any energy, however, it is less likely to happen than the acoustic scattering. The emission of an optical phonon, when the hole is kept in heavy hole band or transit to light hole is only possible to happen when the hole has an energy higher than the optical phonon energy, which for silicon is equal to 0.063eV. Whereas, the transition to split-off band followed by the emission of an optical phonon is only possible when the hole energy is higher than 0.107eV, which is the sum of the optical phonon energy and the spin-orbit splitting energy.

Figure 4.8 - Nonpolar optical phonon scattering rates for holes scattered from the light hole band in Si.

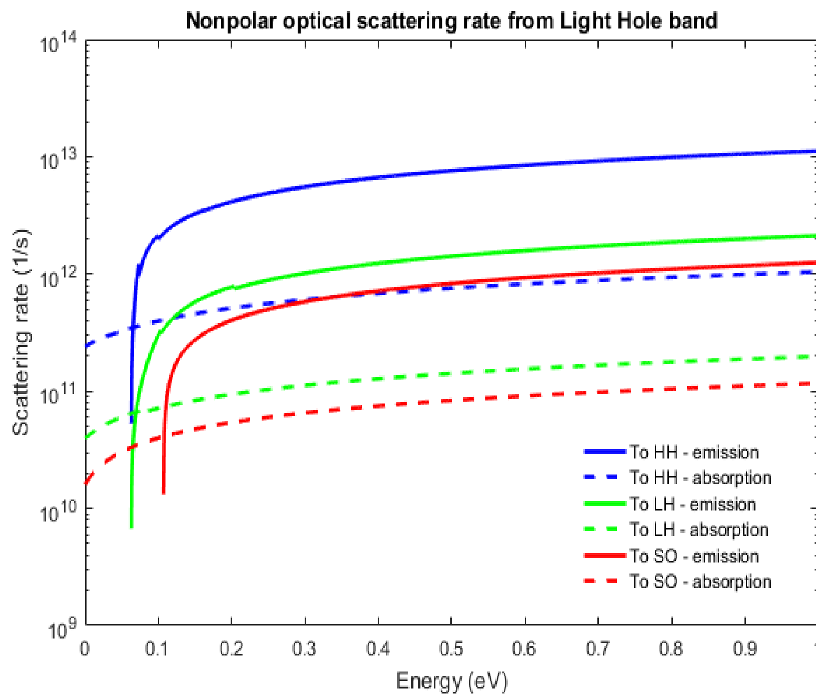

Source: Author

Figure 4.8 shows the optical scattering rates for holes that transit from the light hole band to the light hole, heavy hole and split-off band. In light hole band, the acoustic scattering and both intraband and interband scattering due the absorption of optical phonon can occur at any energy. A hole in this band can only emit an optical phonon and transit to heavy hole or stay in light hole if its energy is higher than 0.063eV. To transit to split-off and emit an optical phonon, the hole must have an energy higher than 0.107eV. The absorption of an optical phonon

followed by a transition to heavy hole band is the scattering mechanism that has the highest probability to happen when the hole energy is smaller than 0.009eV. Acoustic scattering is the most probable one when the hole has an energy between 0.01 and 0.09eV. The emission of an optical phonon followed by a transition to heavy hole band is more likely to happen with holes that have energy higher than 0.1eV.

Figure 4.9 - Nonpolar optical phonon scattering rates for holes scattered from the split-off band in Si.

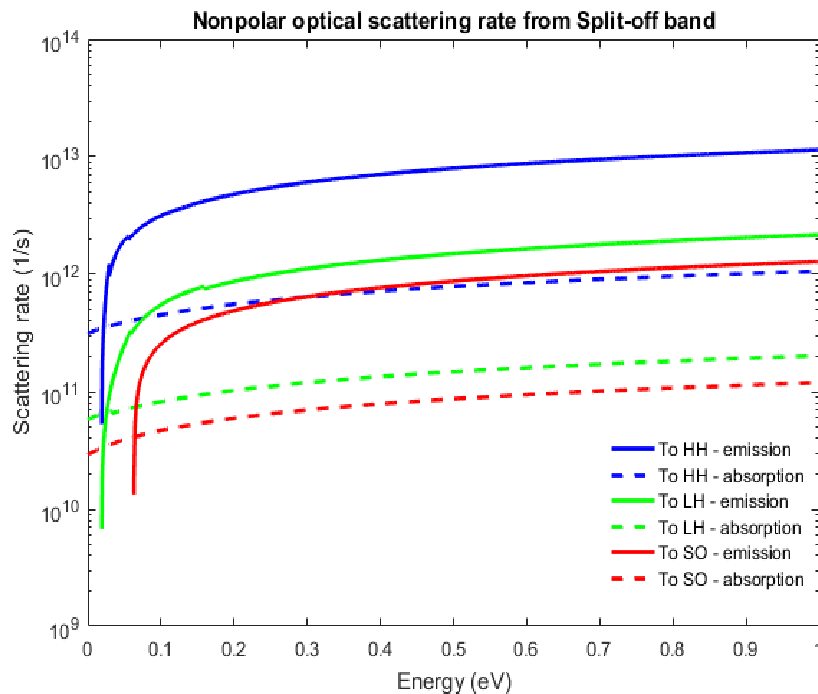

Source: Author

Figure 4.9 shows the optical scattering rates for holes that transit from split-off band to the heavy hole, light hole and split-off band. In the split-off band, the acoustic scattering and both intraband and interband scattering due the absorption of optical phonon can occur at any energy.

A hole in this band can only emit an optical phonon and transit to heavy hole or light hole if its energy is higher than 0.019eV. An intraband optical scattering followed by the emission of an optical phonon only occur to holes with energy higher than 0.063eV. When the hole energy is smaller than 0.02eV, the absorption of an optical phonon followed by a transition to heavy hole band is the most probable scattering mechanism. For holes with energy higher than that, the emission of an optical phonon followed by a transition to heavy hole band is the most probable one.

At low electric field, the mean energy of the hole is around 0.04eV, and the acoustic scattering is more likely to happen than the intraband and interband nonpolar optical scattering in both heavy hole and light hole bands. The acoustic scattering rate may be underestimated when the acoustic scattering is considered an elastic mechanism and the adiabatic approximation is employed to describe the phonon population. Since this scattering mechanism is more important at low energy, the impact of the simplified acoustic scattering is more pronounced, explaining why the drift velocity obtained by the EMC simulation is higher than experimental results in low fields.

The hole velocity at low fields were in better agreement with the experimental results when the acoustic deformation potential constant was increased, however, the velocity in higher fields was also diminished. To overcome this issue, two different values of the acoustic deformation constant could be used, or a more complex description of the acoustic phonon could be employed. Since the interest is simulating the transport of holes in SiGe alloys – where their acoustic branch is described as a combination of the acoustic branch of pure Si and Ge and their optical branch is composed by the Si-Si and Ge-Ge modes – the deformation constants that were used to obtain the results shown in Figure 4.1 are reasonable to evaluate the scattering rates due the presence of silicon in the alloy. In addition, in SiGe alloys, the alloy scattering is more probable to happen than the phonon scattering, diminishing the importance of the acoustic scattering in the transport of holes in SiGe.

Table 4.1 presents the parameters employed in the simulation of transport of holes in silicon. Those constants are related with the description of the physical properties, band structure and the optical and acoustic scattering rates of silicon.

Table 4.1 - Parameters used in Silicon simulations.

Density (kg/m^3)	2329
Sound longitudinal velocity (m/s)	9000
|A|	4.22
|B|	0.78
|C|	4.80
Split-off hole effective mass	0.15m_0
Optical phonon energy (eV)	0.063
E_{ac} (eV)	6.9231
D_{op} (eV/m)	5.2x10^{10}

Source: Author.

4.2 Germanium Transport Simulation

To find the value of the acoustic potential deformation constant and optical potential deformation constant of germanium, a set of simulations was performed, using the same methodology employed to determine silicon constants. After substituting the chosen constants in the simulation code, the hole velocities achieved by simulations should agree with experimental results. The simulations were performed at 220K, because this was the maximum temperature where experimental data was available for hole drift velocity in germanium. The electrical field in experimental results varied from 10^2 to 10^4V/cm, then the same range of electric field was used in the simulations. Both experiments and simulations were performed applying an electric field parallel to [100] direction. The total time of the simulations was set to 10ps.

Figure 4.10 shows the results of hole drift velocity in germanium obtained using the described simulator and experimentally (REGGIANI et. al., 1977) versus the electric field. In the simulation, 20,000 holes were considered. As it is shown in Figure 4.10, the hole velocity is well described in the whole range of electric field. The mean energy of holes was evaluated in these simulations. Figure 4.11 shows the hole energy versus the electric field.

Figure 4.10 - Comparison between the simulated drift velocity of holes in germanium with experimental data.

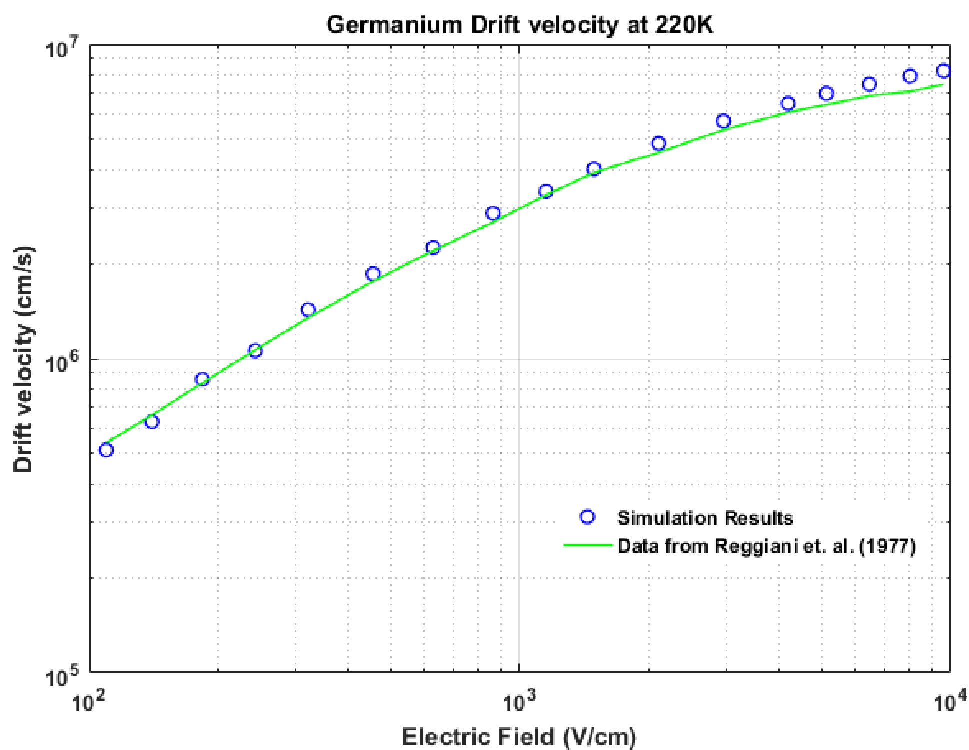

Source: Author

Figure 4.11 – Mean energy of the holes versus electric field for germanium bulk

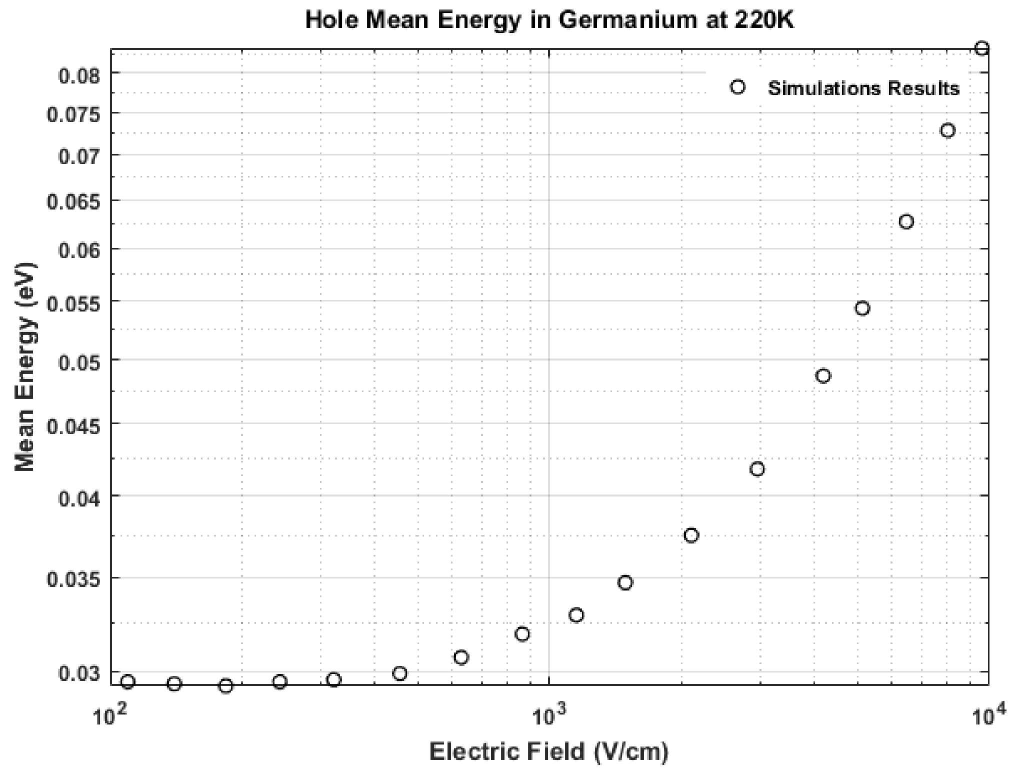

Source: Author

Figure 4.12 - Occupation of the valence bands vs electric field for Ge at 220K.

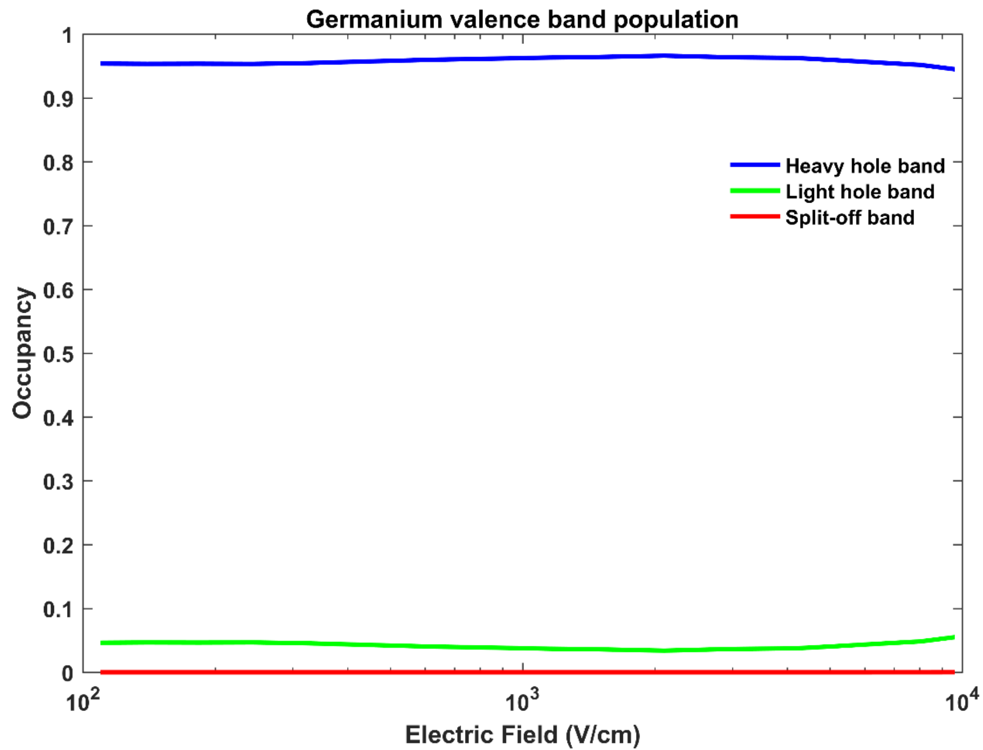

Source: Author

The graphic depicted in Figure 4.12 shows the band occupancy of germanium as a function of the applied electric field. Initially, all the holes are in the heavy hole band. Light hole band eventually become occupied due to nonpolar optical phonon scattering events, nevertheless, more than 90% of the holes stay in the heavy hole band, even for the highest electric field. The split-off band is empty in almost the entire electric field range due to the high spin-orbit splitting energy of germanium, which is 0.29eV. The split-off band becomes slightly occupied at electric fields around 10^4V/cm.

Simulations were performed to obtain the profile of the transient velocity of holes in germanium. These simulations were made at 220K to describe the time evolution of drift velocity and energy of holes in Ge bulk. The time evolution of the energy of holes for electric fields of 15, 25, 50, 75 kV/cm is depicted in Figure 4.13. Those curves show the increase of charge carrier energy due to the external electrical field and until a steady state is reached.

Figure 4.13 - Energy of holes in germanium for applied fields of 15, 25, 50, 75kV/cm.

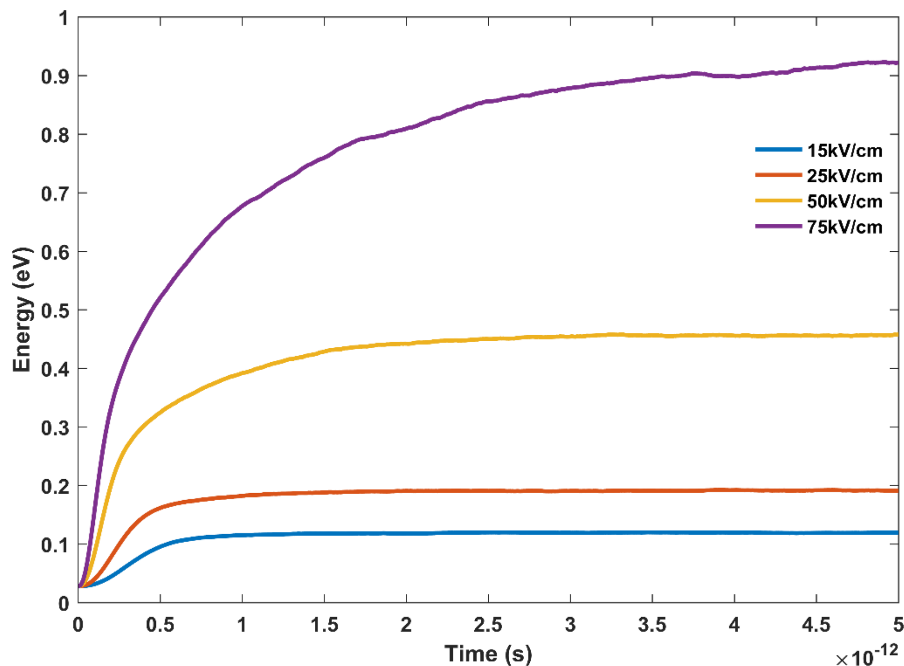

Source: author.

Figure 4.14 shows the time evolution of the drift velocity of holes for electric fields of 15, 25, 50, 75kV/cm. For germanium, the velocity overshoot effect can also be observed at the beginning of the simulation.

Figure 4.14 - Time evolution of drift velocity of holes in silicon for applied fields of 15, 25, 50, 75kV/cm.

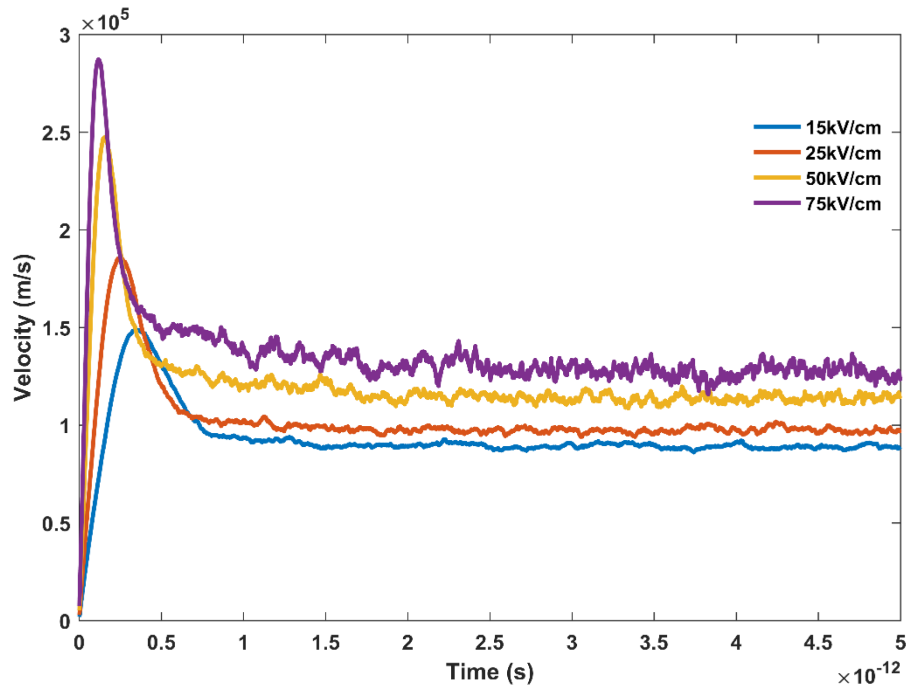

Source: author.

Figure 4.15 shows the acoustic scattering rates for the three valence bands of germanium at 220K. Since the acoustic scattering is modeled as an intraband mechanism, the final band is the same as the initial band.

Figure 4.15 - Acoustic phonon scattering rates for holes in the heavy hole, light hole and split-off bands in Ge.

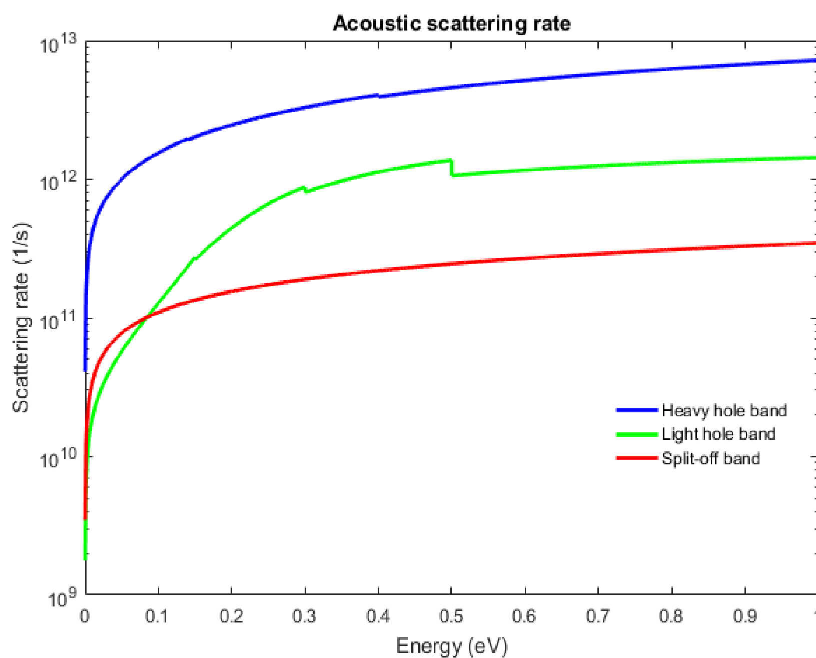

Source: Author

Figure 4.16 - Nonpolar optical phonon scattering rates for holes scattered from the heavy hole band in Ge.

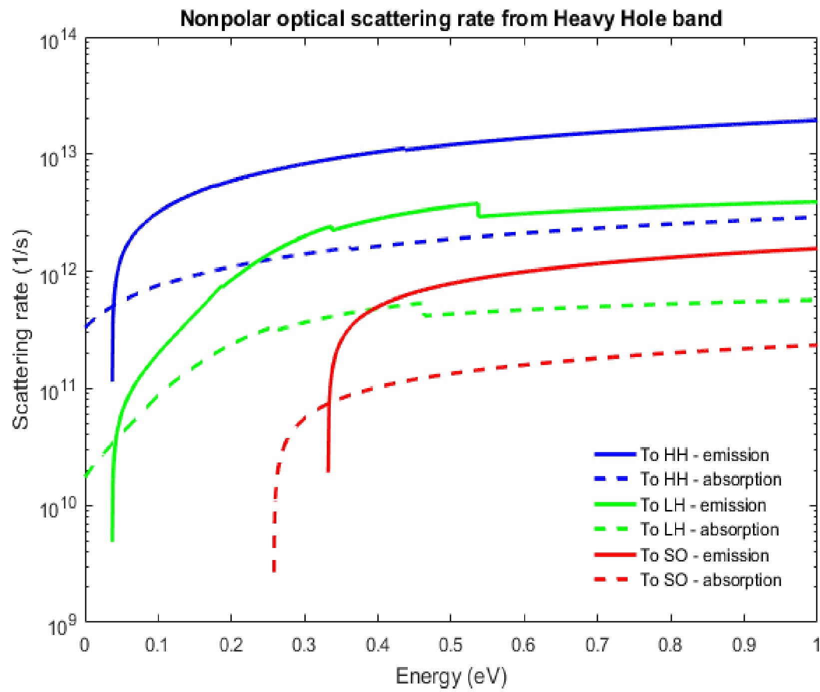

Source: Author

Figure 4.17 - Nonpolar optical phonon scattering rates for holes scattered from the light hole band in Ge.

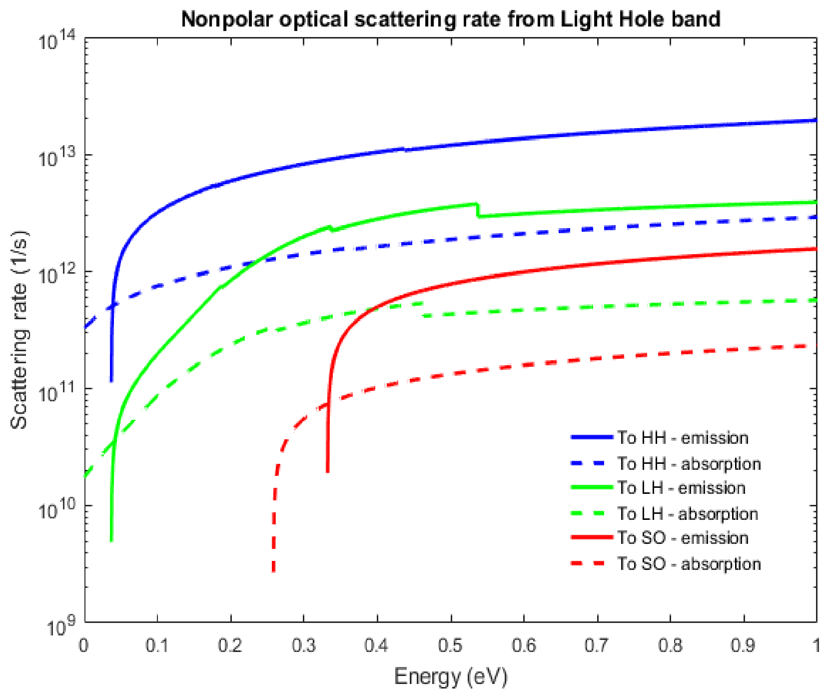

Source: Author

Figure 4.16 shows the optical scattering rates for holes that transit from heavy hole to light hole, split-off and heavy hole band. Figure 4.17 presents the optical scattering rates for holes that transit from light hole to light hole, split-off band and heavy hole band. For heavy hole and light hole band, the optical scattering due absorption and the acoustic scattering can occur at any energy. However, to transit to light hole or heavy hole band due the emission of an optical phonon, the hole must have energy higher than the phonon energy, which for germanium is equal to 0.037eV. To transit to split-off band by emitting an optical phonon, the hole must have an energy higher than 0.327eV.

For holes in heavy hole band with energy lower than 0.008eV, the most likely scattering mechanism is the absorption of an optical phonon due an intraband scattering. Holes with energy between 0.008 and 0.04 are most probable to suffer an acoustic scattering, while holes with energy higher than that are most likely to emit an optical phonon due to an optical phonon intraband scattering.

Holes in light hole band with energy lower than 0.04eV are most likely to transit to heavy hole band due the absorption of an optical phonon, while holes with energy higher than that, are most likely to emit an optical phonon followed by a transition to heavy hole band.

Figure 4.18 - Nonpolar optical phonon scattering rates for holes scattered from the split-off band in Ge.

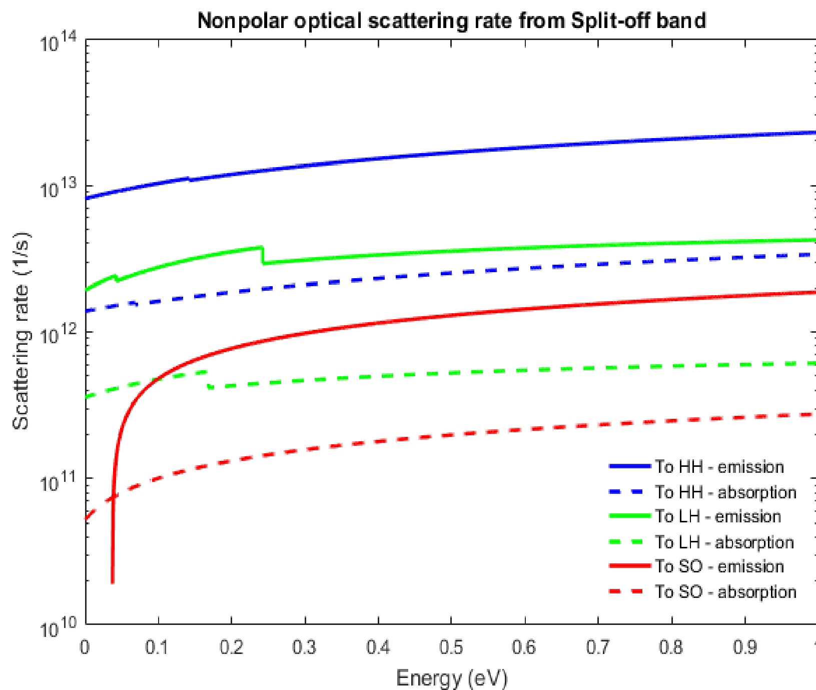

Source: Author

Figure 4.18 shows the optical scattering rates for holes that transit from split-off band to heavy-hole, light-hole and split-off band. The optical scattering due to absorption and the acoustic scattering can occur at any energy, as well as in heavy hole and light hole. For holes in split-off band, for the entire range of energy, the most likely scattering is the emission of an optical phonon followed by a transition to the heavy hole band. Table 4.2 presents the parameters employed in the simulation of transport of holes in germanium. Those parameters are physical constants, band structure related constants and the constants used to calculate the acoustic scattering rate and the nonpolar scattering rates.

Table 4.2 - Parameters used in germanium simulations.

Density (kg/m^3)	5320
Sound longitudinal velocity (m/s)	5400
$\|A\|$	13.38
$\|B\|$	8.48
$\|C\|$	13.14
Split-off hole effective mass	$0.075m_0$
Optical phonon energy (eV)	0.037
E_{ac} (eV)	5.1508
D_{op} (eV/m)	$1.18x10^{11}$

Source: Author.

4.3 SiGe Transport Simulations

The mobility of holes in SiGe alloys at 300K when exposed to low fields has been studied experimentally (BUSCH; VOGT, 1960) and by simulations (FISCHETTI; LAUX, 1996; MEHROTRA; PAUL; KLIMECK, 2011). In order to study the transport of holes in SiGe alloys and to validate the proposed model, the mobility of holes in these alloys was calculated at 300K and at low fields (10^3V/cm) where the ohmic behavior is still valid. The alloys studied have germanium content equal to 0.1, 0.2, 0.3, 0.4, 0.5, 0.6, 0.7, 0.8 and 0.9.

The split-off band of these alloys was modeled as a parabolic and spherical band. The effective mass of the split-off band of each alloy was estimated by fitting a parabolic function – equation (3.1) – to the EPM split-off band data (GONZALEZ, 2001). The splitting energy of each alloy was obtained from the EPM curve. Both the effective mass of split-off band ant the splitting energy are shown in Table 4.3. Both heavy hole and light hole bands of each alloy was

modeled as a nonparabolic and warped band. The dispersion relation of heavy hole and light hole bands are given, respectively, by equations (3.11) and (3.12) . The Dresselhaus parameters – A, B and C - of each studied alloy are showed in Table 4.3, while the nonparabolicity parameters are demonstrated in the APPENDIX A.

Table 4.3 – Band structure constants of SiGe alloys used in the simulation of hole transport. In the alloys studied, the Ge content varied from 0.1 to 0.9.

Ge content	A	B	C	m_{so} (m_0)	Δ (eV)
0.1	0.85	4.4	4.99	0.1408	0.05879
0.2	0.95	4.65	5.15	0.1402	0.08067
0.3	1.15	4.95	5.3	0.1356	0.1037
0.4	1.3	5.28	5.65	0.1282	0.1283
0.5	1.65	5.55	5.95	0.1189	0.1546
0.6	1.9	6.15	6.9	0.1086	0.1827
0.7	2.8	6.82	7.3	0.0982	0.2121
0.8	4.4	8.35	8.5	0.0889	0.2426
0.9	4.57	8.72	9.25	0.0812	0.2737

Source: Author.

The description of SiGe alloy spectrum can be made by considering an averaged spectrum or by taking into account the coexistence of both Si and Ge modes. In this model, to calculate the acoustic scattering rate, an average acoustic spectrum was considered. The potential deformation, the sound velocity and the density of SiGe alloy was given by linear interpolation between the Si and Ge values, which values are showed in Table 4.1 and Table 4.2, respectively. In the SiGe alloy optical spectrum, both Si-like and Ge-like modes are considered to coexist, thus nonpolar optical scattering rate was calculated for each mode, and the phonon population of each type was weighted according to the appropriate mole fraction, which is $1 - x$ for the Si phonons and x for Ge.

Besides having its trajectory deviated by phonon scattering, holes moving inside these alloys may also be scattered by the lattice defects due to the fluctuation of the alloy concentration. The alloy scattering potential has been reported to be 0.7 (MEHROTRA; PAUL; KLIMECK, 2011), 0.8, 1 (FISCHETTI; LAUX, 1996) and 1.4 (BRIGGS; WALKER; HERBERT, 1998). In this work, the alloy scattering was changed around these values until the profile of the curve mobility versus germanium content had a reasonable agreement with experimental results. The mobility of these alloys was calculated by simulating the transport of

holes exposed to an electric field equal to 10^3 V/cm at 300K and the total time of the simulation was equal to 10ps. The drift velocity of holes was calculated after a steady state was reached. Then, the mobility μ was calculated employing the equation (4.1), which is only valid for the ohmic behavior.

$$\mu = \frac{\langle v_d \rangle}{E} \tag{4.1}$$

In this simulator, the curve mobility versus Ge content that had the best agreement with experimental results was obtained when the alloy scattering potential was equal to 1.5. Nevertheless, a good level of agreement was also obtained for an alloy scattering potential equal to 1.2. Figure 4.19 compares the mobility results obtained by the simulator proposed in this work – when the alloy scattering potential is equal to 1.2 – with experimental results and with the simulation results obtained by Fischetti and Laux (1996), when they used an alloy scattering potential equal to 0.8. In Figure 4.19, the green squares are the results of this work, they agree with the results of Fischetti and Laux (1996) in the entire range of germanium content. However, the mobility of $Si_{0.7}Ge_{0.3}$, $Si_{0.6}Ge_{0.4}$ and $Si_{0.5}Ge_{05}$ deviate from the experimental results. It is observed that the mobility of these alloys is overestimated in comparison to experimental results.

Figure 4.19 – Comparison of the curve hole mobility in $Si_{1-x}Ge_x$ alloys versus germanium content. The scattering potential used in the simulator proposed in this work is equal to 1.2.

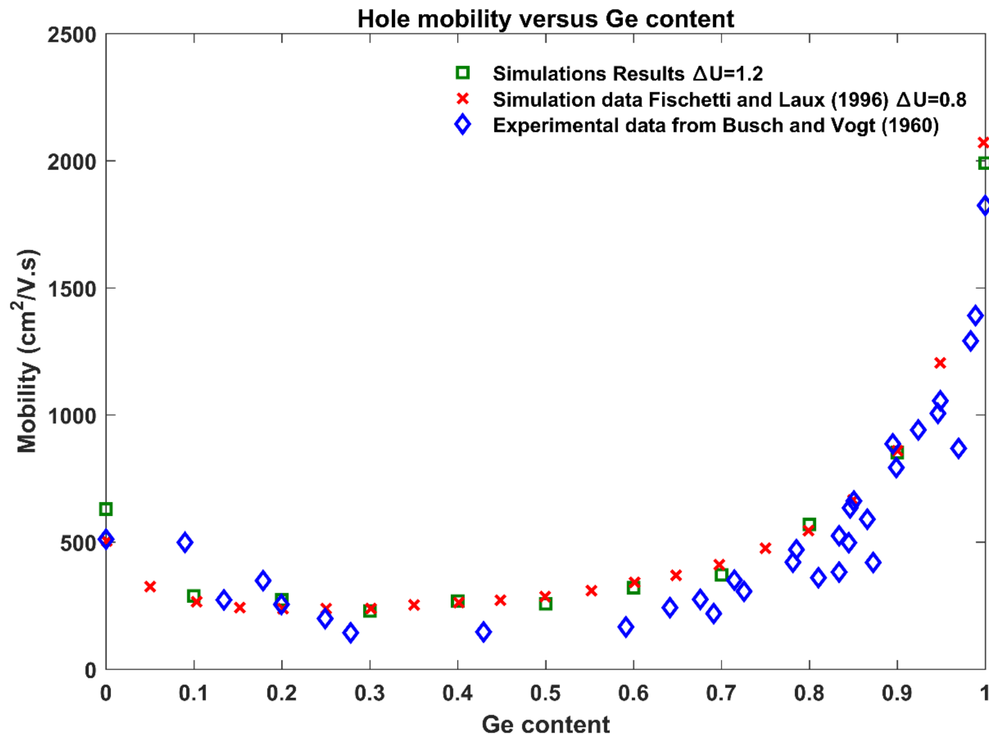

Source: author.

Figure 4.20 compares the mobility results obtained by the simulator proposed in this work - when the alloy scattering potential is equal to 1.5 - with experimental results and with the results obtained by Fischetti and Laux (1996), when they used an alloy scattering potential equal to 1. In Figure 4.20, the green squares are the results of this work, they agree with the results of Fischetti and Laux (1996) in the entire range of germanium content. Besides, it is observed that the mobility of these alloys is in a great agreement to experimental results.

Figure 4.20 - Comparison of the curve hole mobility in $Si_{1-x}Ge_x$ alloys versus germanium content. The scattering potential used in the simulator proposed in this work is equal to 1.5.

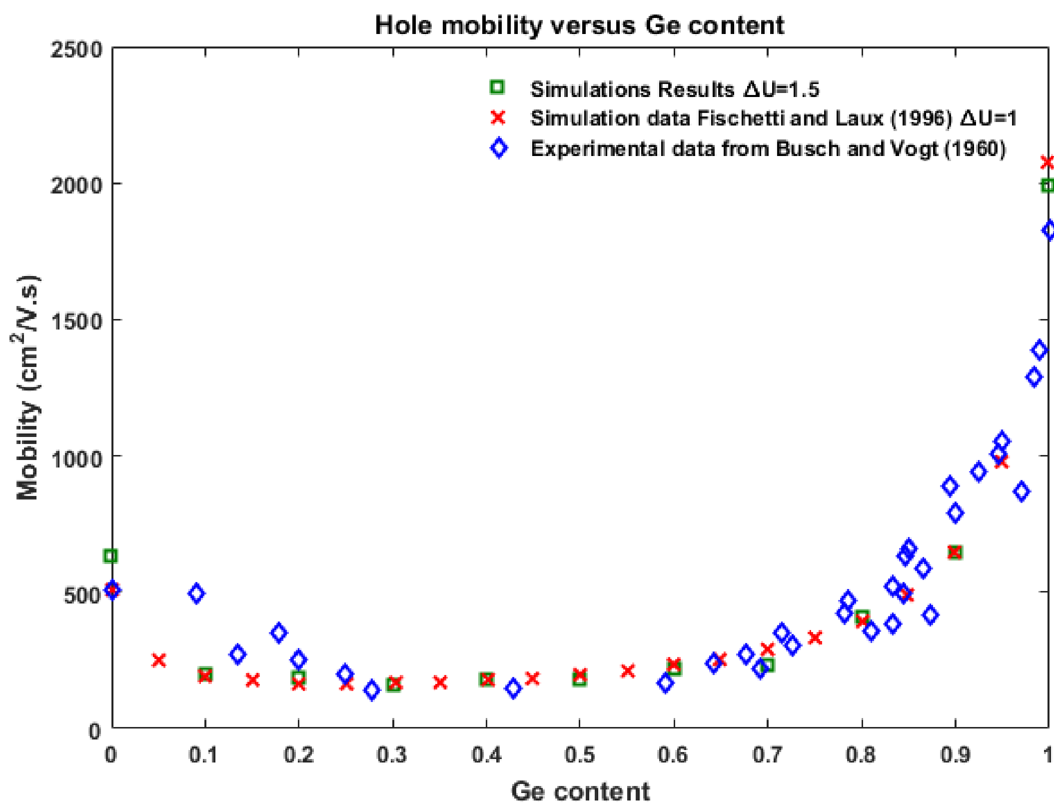

Source: Author.

The proposed simulator of holes transport in SiGe alloys was validated by comparing the results obtained by the simulator with experimental data. Since the hole mobility calculated agrees with the experimental data, a future work is developing from the SiGe bulk simulator a device simulator by adding the Poisson's equation into the bulk code to calculate the electrical potential to which charge carrier are exposed due to the charge distribution in the device.

5 CONCLUSION

This work proposed an Ensemble Monte Carlo simulator to study the hole transport in silicon, germanium and SiGe alloys. To simulate the hole transport, the valence band structure of these materials was modeled using a three-band approach where the light hole and heavy hole band are considered warped and nonparabolic bands, whereas the split-off band is considered spherical and parabolic band. To generate an expression for the dispersion relation of heavy hole and light hole, the warping effect was taken into account by the Dresselhaus, Kip and Kittel (1955) expression, while the nonparabolicity effect was considered by using the analytical function proposed by Rodríguez-Bolívar, Gómez-Campos e Carceller (2004). Both Dresselhaus parameters and nonparabolic constants were determined by fitting the respective expressions to the EPM band structure.

Acoustic phonon scattering and nonpolar optical phonon scattering are the only scattering mechanisms included in the bulk simulator of the pure materials. Acoustic phonon scattering is modeled as an intraband and elastic process, whereas the nonpolar optical scattering is an inelastic process that can be intraband and interband. For silicon and germanium, the deformation potential constants were thoroughly adjusted in order to achieve drift velocity results that agree with the experimental data. In this method, the transport of holes was simulated in a wide range of electric fields where the drift velocity of holes in these materials were estimated, then they were compared with experimental results.

The alloy properties were estimated by using the Virtual Crystal Approach, where the properties of alloys are defined by linearly interpolating the pure properties in accordance with the content of the constituent atoms. In the SiGe alloy simulator, the alloy acoustic phonon spectrum is considered an average of Si and Ge spectrums. Following this approach, the acoustic deformation potential of each alloy is determined by VCA. Whereas, in the optical spectrum of the alloy, both Si-like and Ge-like modes are considered to coexist, thus nonpolar optical scattering rate is calculated for each mode, and the phonon population of each type is weighted according to the appropriate mole fraction, which is $1-x$ for the Si phonons and x for Ge. Besides the phonon scattering there is also the alloy scattering, whose potential was obtained by estimating the low field hole mobility in SiGe alloys with distinct Ge content

The curves that presents the time evolution of velocity and energy of holes inside silicon for different electric fields, in section 4.1, reveals that the simulator is working properly. The drift velocities achieved by the simulator at 300K highly agree with experimental results for electric fields higher than 1.5kV/cm. However, the velocity is overestimated by the simulator

at lower fields. This effect may be generated by the simplifications made when calculating the acoustic scattering rate. This issue is observed only at low fields because this mechanism is highly significant in silicon at 300K at low fields. Considering the results of hole transport in silicon, it is possible to acknowledge that this model adequately simulates the hole transport in silicon at 300K when the electric field is greater than 1.5kV/cm. When it comes to lower fields, the model of acoustic phonon scattering can be enhanced to improve the drift velocity results.

The time evolution curves of velocity and energy for different electric fields at 220K exhibited in section 4.2 guarantee that the simulator of hole transport in Ge is functionable. The results of drift velocity at 220K achieved by the simulator agree with experimental results in the entire range of electric field. By comparing the simulation results to experimental data, it is possible to affirm that the simulator successfully simulates the transport of holes in germanium at 220K.

The SiGe alloy simulator was validated by calculating the low field mobility of holes in these alloys at 300K. The mobility achieved in this simulator was compared with previous simulation results and with experimental results, demonstrating that the results obtained by the simulator is in great agreement with both simulation and experimental results in the whole range of germanium content. Therefore, it is possible to assume the SiGe alloy simulator proposed in this work is suitable to simulate the transport of holes in low electric fields and at 300K.

Since the bulk simulator of SiGe is already functionable, a device simulator SiGe transistors can be developed from the bulk simulator adding the Poisson's equation into the code in order to calculate the potential to which charge carrier are exposed due to charge distribution in the device. In this approach, BTE and Poisson's equation are solved in a self-consistently way.

This device simulator can be employed to estimate the effect of Random Dopant Fluctuation (RDF) and Random Trapping on SiGe transistors (ROSSETTO, 2018). Random Dopant Fluctuation (RDF) is the source of variability that comes from the random distribution of dopant atoms in the channel of a transistor. While traps are charge trapping states randomly distributed in the oxide and in the surface between oxide and gate material. Traps can either emit or capture charge carriers and both events are stochastic processes. These two effects impact the transistor electrical properties such threshold voltage and drain current.

REFERENCES

ASCHROFT, N. W., MERMIN, N. D., **Solid State Physics**. Philadelphia,PA: Saunders College Publishing, 1976.

BRIGGS, P. J.; WALKER, A. B.; HERBERT, D. C. Calculation of hole mobilities in relaxed and strained SiGe by Monte Carlo simulation. **Semiconductor Science and Technology**, [s.l.], v. 13, p. 680-691, 1998.

BUSCH, G.; VOGT, O. Elektrische Leitfähigkeit und Halleffekt von Ge-Si-Legierungen. **Helvetica Physica Acta.** v. 33. p. 437-458, 1960.

CALLISTER JR, W. D. Phase Diagrams. In: **Fundamentals of Materials Science and Engineering**. 5th edition. John Wiley & Sons, Inc. [s.l.], 2001. p. 281-315.

CAMARGO, V. V. A. **Evaluating the Impact of Charge Traps on MOSFETs and Circuits**. Dissertation (Doctorate in Microelectronics) - Universidade Federal do Rio Grande do Sul, Porto Alegre, Brasil, 2016.

COHEN, M. L; LOUIE, S. G. **Fundamentals of Condensed Matter Physics**. 1st Ed. Cambridge, United Kingdom: Cambridge University Press, 2016.

DEWEY, J., OSMAN, M. A. Monte Carlo study of hole transport in silicon. **Journal of applied physics**, v. 74, n. 5, p. 3219-3223, 1993.

DRESSELHAUS, G. KIP, A. F.; KITTEL, C. Cyclotron Resonance of Electrons and Holes in Silicon and Gerii1anium Crystals. **Physical. Review**, [s.l.], v. **98**, n. 2, p. 368-384, 1955.

DUNN, W. L., SHULTIS, J. K. **Exploring Monte Carlo Methods**. Elsevier, 2012.

FISCHETTI, M. V.; LAUX, S. E. Band structure, deformation potentials, and carrier mobility in strained Si, Ge, and SiGe alloys. **Journal Of Applied Physics**, [s.l.], v. 80, n. 4, p.2234-2252, 15 ago. 1996. AIP Publishing. http://dx.doi.org/10.1063/1.363052.

FRANCO, J. et al. On the impact of the Si passivation layer thickness on the NBTI of nanoscaled Si0:45Ge0:55 pMOSFETs. **Microelectronic Engineering**, v. 88, n. 7, p.1388–1391, 2011.

GILLESPIE, B. A. **Bond Order Potentials for Group IV Semiconductors.** 2009. 183 f. Dissertation (Doctorate in Engineering Physics) - University of Virginia, 2009.

GONZALEZ, S. **Empirical pseudopotential method for the band structure calculation of strained Si1-xGex materials**. Thesis (Master of Science) - Arizona State University, Tempe, AZ, 2001.

HAMAGUCHI, C. **Basic Semiconductor Physics**. New York: Springer, 2001.

HATHWAR, R. **Generalized Monte Carlo Tool for Investigating Low-Field and High Field Properties of Materials Using Non-parabolic Band Structure Model**. Thesis (Master of Science) Arizona State University, June 2011

HERRING, C. A New Method for Calculating Wave Functions in Crystals. **Physical Review,** [s.l.], v. 57, n. 12, p.1169-1177, 15 jun. 1940. American Physical Society (APS). http://dx.doi.org/10.1103/physrev.57.1169.

JACOBONI, C. **Theory of Electron Transport in Semiconductors**: A Pathway from Elementary Physics to Nonequilibrium Green Functions. Springer, 2010.

JACOBONI, C., LUGLI, P. **The Monte Carlo Method for Semiconductor Device Simulation**. First edition. Springer-Verlag, New York, 1989.

JACOBONI, C. et al. A review of some charge transport properties of silicon. **Solid-State Electronics**, v. 20, n. 2, p. 77-89, 1977.

KANO, K. **Semiconductor Devices**. New Jersey: Prentice Hall, 1998.

KASAP, S. and CAPPER, P. **Springer Handbook of Electronic and Photonic Materials**. Springer, 2006.

KRISHNAN, S. **Band-structure and Detailed Quantum Effects on Hole Transport in P-channel MOSFETs.** Dissertation (Doctorate of Philosophy) - Arizona State University, Tempe, AZ, 2005.

LUNDSTROM, M. **Fundamentals of Carrier Transport**. Cambridge, U.K: Cambridge University Press, 2000.

MARTIN, R. M.; REINING, L.; CEPERLEY, D. M. **Interacting electrons: Theory and computational approaches.** 1st ed. United Kingdom: Cambridge University Press, 2016.

MECHOLSKY, Nicholas A. et al. Density of States for Warped Energy Bands. **Scientific Reports**, [s.l.], v. 6, n. 1, p.1-9, 24 fev. 2016. Springer Science and Business Media LLC. http://dx.doi.org/10.1038/srep22098.

MEHROTRA, S. R.; PAUL, A.; KLIMECK, G. Atomistic approach to alloy scattering in Si1−xGex. **Applied Physics Letters**, [s.l.], v. 98, n. 17, p.1-3, 25 abr. 2011. AIP Publishing. http://dx.doi.org/10.1063/1.3583983.

MOORE, G.E. Progress in Digital Integrated Electronics. **Proc. Technical Digest Intel Electron Devices Meeting**, vol. 21, pp. 11–13, 1975.

REIF, F. **Fundamentals of Statistical and Thermal Physics**. London, U.K.: McGraw-Hill, 1985.

FERRY, D. K. **Semiconductors: Bonds and bands**. Institute of Physics Publishing, [s.l], 2013.

REGGIANI, L. et al. Hole drift velocity in germanium. **Physical Review B**, [s.l] v. 16, n. 6, p.2781-2791, set. 1977.

RODRÍGUEZ-BOLÍVAR, S; GÓMEZ-CAMPOS, F M; CARCELLER, J. Simple analytical valence band structure including warping and non-parabolicity to investigate hole transport in Si and Ge. **Semiconductor Science and Technology**, [s.l.], v. 20, n. 1, p.16-22, 27 nov. 2004. IOP Publishing. http://dx.doi.org/10.1088/0268-1242/20/1/003.

RODRÍGUEZ-BOLÍVAR, S. et al. Implications of nonparabolicity, warping, and inelastic phonon scattering on hole transport in pure Si and Ge within the effective mass framework. **Journal of Applied Physics,** [s.l.], v. 97, n. 1, p.1-10, jan. 2005. AIP Publishing. http://dx.doi.org/10.1063/1.1823025.

ROSSETTO, A. C. **Modeling and Simulation of Self-heating Effects in p-type MOS Transistors.** Dissertation (Doctorate in Microelectronics) - Universidade Federal do Rio Grande do Sul, Porto Alegre, Brasil, 2018.

SÓLYOM, J. **Fundamentals of the Physics of Solids. V.1 – Structure and Dynamics**. Springer-Verlag Berlin Heidelberg, 2007

SÓLYOM, J. **Fundamentals of the Physics of Solids. V.3 - Normal, Broken-Symmetry, and Correlated Systems**. Springer-Verlag Berlin Heidelberg, 2010.

THEIS, T. N. and WONG, P.: **The End of Moore's Law: A New Beginning for Information Technology**. IEEE CS and the AIP, 2016.

VASILESKA, D., GOODNICK S. M. and KLIMECK, G.: **Computational Electronics: From Semi-Classical to Quantum Transport Modeling**, CRC Press, June 2010

VASILESKA, D., GOODNICK S. M.: **Computational Electronics**, Morgan and Claypool Publishers, 2006.

SHIMA, M.: Strained-SiGe-channel p-MOSFET with enhanced hole mobility and lower parasitic resistance, **J. Fujitsu Sci. Tech**., 39, 1. 2003.

WALTL, M. et al.: Superior NBTI In High-K Sige Transistors–Part II: Theory. **IEEE Transactions on Electron Devices**, Vol. 64, No. 5, 2099-2105, May 2017.

WHALL, T. E.; PARKER, E. H. C. SiGe heterostructures for FET applications. **Journal of Physics. D: Applied Physics**. v. 31. p. 1397–1416, 1998.

XIAOJIANG, He, "**Two-Dimensional Monte Carlo Simulations of Ultra-Small MOSFETs**", MS Thesis, Arizona State University, May 2000

YU P. Y.; CARDONA, M. **Fundamentals of Semiconductors:** Physics and Materials Properties, 4th. Ed. Heidelberg: Springer, 2010.

APPENDIX A

The analytical expression that describes the nonparabolicity of heavy-hole and light-hole bands as a function of the energy is given by (RODRÍGUEZ-BOLÍVAR; GÓMEZ-CAMPOS; CARCELLER, 2004):

$$\chi(E) = \frac{aE^2 + bE + c}{dE + 1} \tag{A.1}$$

The parameters *a, b, c* and *d* of the nonparabolicity function of the heavy-hole and light-hole band of silicon, of the SiGe alloys and of germanium are shown in Table A. 1 - Table A. 22. They were obtained by the fitting process explained in section 3.2.2.

Table A. 1 - Si heavy hole band.

Energy range (eV)	a (eV^{-2})	b (eV^{-1})	c	d (eV^{-1})
0-0.01	-19.3	2.4	0.9	50
0.01-0.0365	55.14	5.73	0.7	20
0.0365-0.11	10.574	17.96	0.8	37.8
0.11-1.0	0.0629	20.8347	0.75	39.5

Table A. 2 - Si light hole band.

Energy range (eV)	a (eV^{-2})	b (eV^{-1})	c	d (eV^{-1})
0-0.04	-54.11	8.79	1.034	22.38
0.04-0.14	8.2	29.8	1.518	72
0.14-1.0	-0.06032	13.16	0.77	28.1

Table A. 3 - $Si_{0.9}Ge_{0.1}$ heavy hole band

Energy range (eV)	a (eV^{-2})	b (eV^{-1})	c	d (eV^{-1})
0-0.05	9.866	5	1	12
0.05-0.1	5.185	2.4	0.92	6
0.1-1.0	-0.15	5.21	0.98	8.968

Table A. 4 - $Si_{0.9}Ge_{0.1}$ light hole band

Energy range (eV)	a (eV^{-2})	b (eV^{-1})	c	d (eV^{-1})
0-0.03	0.005	9.82	0.75	20
0.03-0.07	0.02	13.2	0.78	25.48
0.07-1.0	-0.00388	4.157	0.95	12.83

Table A. 5 - $Si_{0.8}Ge_{0.2}$ heavy hole band

Energy range (eV)	a (eV^{-2})	b (eV^{-1})	c	d (eV^{-1})
0-0.05	5.1	2.06	1.09	6.842
0.05-0.1	-0.0069	3.475	1.05	6.58
0.1-1.0	-0.1544	9.584	1.2	15.4815

Table A. 6 - $Si_{0.8}Ge_{0.2}$ light hole band

Energy range (eV)	a (eV^{-2})	b (eV^{-1})	c	d (eV^{-1})
0-0.03	-207.8	20.9	1	26.2
0.03-0.1	-8.792	28.91	1.663	60.87
0.1-1.0	0.063	4.397	0.9931	12.46

Table A. 7 - $Si_{0.7}Ge_{0.3}$ heavy hole band

Energy range (eV)	a (eV^{-2})	b (eV^{-1})	c	d (eV^{-1})
0-0.05	2.8	2.05	0.98	5.502
0.05-0.1	5.7968	5.5	1	10.1
0.1-1.0	-0.1544	9.5	1.07	14.8

Table A.8 - $Si_{0.7}Ge_{0.3}$ light hole band

Energy range (eV)	a (eV^{-2})	b (eV^{-1})	c	d (eV^{-1})
0-0.05	-90.03	9.788	1.1	12.98
0.05-0.1	-12.92	20.42	1.524	39.6
0.1-1.0	-0.0179	4.222	1.15	11.7

Table A. 9 - $Si_{0.6}Ge_{0.4}$ heavy hole band

Energy range (eV)	a (eV^{-2})	b (eV^{-1})	c	d (eV^{-1})
0-0.05	0.107	3.01	0.95	5.2
0.05-0.1	-13.82	22.41	1.048	28.14
0.1-1.0	-0.1065	2.95	0.95	4.8

Table A. 10 - $Si_{0.6}Ge_{0.4}$ light hole band

Energy range (eV)	a (eV^{-2})	b (eV^{-1})	c	d (eV^{-1})
0-0.05	-47.42	3.642	1.083	4.857
0.05-0.1	0.66	1.231	1.2	7.314
0.1-1.0	-0.0129	3.78	1.18	9.98

Table A.11 - $Si_{0.5}Ge_{0.5}$ heavy hole band

Energy range (eV)	a (eV^{-2})	b (eV^{-1})	c	d (eV^{-1})
0-0.05	5.2070	10.573	1.065	15.211
0.05-0.1	5.122	10	1.1	15
0.1-1.0	-0.11	3.587	1	5.717

Table A. 12 - $Si_{0.5}Ge_{0.5}$ light hole band

Energy range (eV)	a (eV^{-2})	b (eV^{-1})	c	d (eV^{-1})
0-0.05	-48.42	4	0.98	3.6
0.05-0.1	0.7	1.4	1.18	7.38
0.1-1.0	-0.095	3.15	1.02	7.29

Table A. 13 - $Si_{0.4}Ge_{0.6}$ heavy hole band

Energy range (eV)	a (eV^{-2})	b (eV^{-1})	c	d (eV^{-1})
0-0.05	2.99	2.425	1.01	4.45
0.05-0.1	-0.4044	1.78	0.99	3.09
0.1-1.0	-0.1207	2.461	0.98	3.6747

Table A. 14 - $Si_{0.4}Ge_{0.6}$ light hole band

Energy range (eV)	a (eV^{-2})	b (eV^{-1})	c	d (eV^{-1})
0-0.05	-13.03	-1.973	1.05	1.376
0.05-0.1	1.44	1.79	1.07	6.79
0.1-1.0	-0.0098	4.395	1.09	10.16

Table A. 15 - $Si_{0.3}Ge_{0.7}$ heavy hole band

Energy range (eV)	a (eV^{-2})	b (eV^{-1})	c	d (eV^{-1})
0-0.05	-9.4	6.5	1.02	7.43
0.05-0.1	0.6696	2.35	1.01	3.406
0.1-1.0	-0.13	2.45	1.04	3.58

Table A. 16 - $Si_{0.3}Ge_{0.7}$ light hole band

Energy range (eV)	a (eV^{-2})	b (eV^{-1})	c	d (eV^{-1})
0-0.05	-9.799	2.9	0.95	4.5953
0.05-0.1	2.5	5.5	1.15	11.9
0.1-1.0	-0.0469	3.367	1.1	8.03

Table A. 17 - $Si_{0.2}Ge_{0.8}$ heavy hole band

Energy range (eV)	a (eV^{-2})	b (eV^{-1})	c	d (eV^{-1})
0-0.05	-10.64	15.61	1.12	16.03
0.05-0.1	-0.1682	2.1793	1.142	3.5961
0.1-1.0	-0.1339	3.2	1.15	4.67

Table A. 18 - $Si_{0.2}Ge_{0.8}$ light hole band

Energy range (eV)	a (eV^{-2})	b (eV^{-1})	c	d (eV^{-1})
0-0.1	-5.363	2.8	1.08	6.3
0.1-0.3	-1.711	4.8	1.2	10.74
0.3-1.0	-0.027	4.1	1.27	10.7

Table A. 19 - $Si_{0.1}Ge_{0.9}$ heavy hole band

Energy range (eV)	a (eV^{-2})	b (eV^{-1})	c	d (eV^{-1})
0-0.05	-10.4	14.71	1.14	15.09
0.05-0.1	-0.17	2.18	1.14	3.6
0.1-1.0	-0.217	3.9	1.1	4.732

Table A. 20 - $Si_{0.1}Ge_{0.9}$ light hole band

Energy range (eV)	a (eV^{-2})	b (eV^{-1})	c	d (eV^{-1})
0-0.1	-160.1	53.52	1.181	47.79
0.1-0.3	-1.333	3.715	1.446	10.562
0.3-1.0	-0.0031	3.05	0.96	7.2

Table A. 21 - Ge heavy hole band

Energy range (eV)	a (eV^{-2})	b (eV^{-1})	c	d (eV^{-1})
0-0.05	3.054	-5.396	0.8859	-5.473
0.05-0.14	-0.6163	0.819	0.886	1.652
0.14-0.4	-0.00196	0.9628	0.8864	1.936
0.4-1.0	-0.00119	1.3	0.8864	2.353

Table A. 22 - Ge light hole band

Energy range (eV)	a (eV^{-2})	b (eV^{-1})	c	d (eV^{-1})
0-0.15	-28.67	7.377	0.879	10.89
0.15-0.3	4.166	-2.99	1.159	3.819
0.3-0.5	1.82	0.15	1.55	16.4
0.5-1.0	0.82	8.24	1.08	45.2